Numerical simulations of the evolution of astrospheres in different interstellar conditions

D.V. Moyeni

orcid.org/0000-0002-7613-9928

Dissertation accepted in partial fulfilment of the requirements for the degree *Master of Science in Astrophysical Sciences* at the North-West University

Supervisor: Prof S.E.S Ferreira

Graduation May 2024

27724204

Acknowledgements

I dedicate this dissertation to my parents, Kebitsamang and Mosimanegape Moyeni. Nobody has been more important to me in the pursuit of my goals than the members of my family. Please accept my most heartfelt appreciation. Thank you for the love, guidance, and support you provided. You are the ultimate role models. Chances are that you thought I did not notice, but thank you for the sacrifices you made to enable me to study. Thank you both for giving me strength to reach for the stars and chase my dreams.

My deepest gratitude and appreciation goes to my advisor, Prof. S.E.S Ferreira, for his unwavering support, guidance, and invaluable insights throughout this research work.

I extend my sincere thanks to Prof. Yurko Sushch, Prof. Illani Loubser, Dr Ephrem Tesfaye, Dr Katlego Moloto, Dr Klaus Scherer, Mr. Jaundré Light, Mr Dakalo Phuravhathu, and the Helio Journal Group. Their expertise and enthusiasm were instrumental in navigating challenges and achieving meaningful outcomes.

Special thanks go to Mr Lendl Fransman, Mrs Elanie van Rooyan, and Mrs Lee-Ann van Wyk for administrative assistance and to Mr Mathew Holleran, Mr Khotso Tefo, and Mr Masego Mosiane for providing computer and office-related equipment.

I am grateful to the North-West University, NRF and NASSP for providing resources, finance, and a conducive research environment.

I extend my appreciation to Prof. Christo Venter, Mr George Mbewe, Mr Dumiso Mithi, Mr Motseothata Tiisang, Mr Salomon van Niekerk, Mr Wiseman Shungube, and Miss Jane Letsoalo for their support and engaging conversations.

Special thanks go to Mr Tlamelo Nkhutleng for his continuous support throughout the research.

I am much obliged to Mr Andile Nkosi for the encouragement to continue with physics.

Ms Jennifer Wessels, for editing, and proofreading my dissertation.

Finally, my heartfelt thanks to Ms Pauline Masoa for her constant love; support, motivation and patience.

Abstract

Astrospheres are large-scale structures arising from the interaction between the stellar wind and the interstellar medium (ISM). This study investigates the effect of various parameters, such as the simulation time, mass loss rate, ISM density, ISM temperature, and ISM magnetic field, on the evolution of an astrosphere using the two-dimensional magnetohydrodynamic model of Fahr and Kausch (2000). The emphasis is on calculating the density profile, bow shock (BS) compression ratio, speed, and BS width as the stellar wind (SW) expands into the ISM. Results show that later simulation times lead to a more developed astrosphere with a thin outer shell forming, the thickness of which depends on the radiative cooling process. The mass loss rate affects the size of the astrosphere, with higher rates resulting in larger astrospheric structures. The ISM density also influences the size of the astrospheric cavity and the radiative cooling process. The ISM magnetic field can either expand or compress the outer structure of the astrosphere, depending on its orientation. The study also investigates the astrosphere of λ Cephei. λ Cephei is a bright runaway star. Simulations of Baalmann et al. (2021) show the position of the termination shock (TS), astropause (AP), and bow shock (BS) of λ Cephei. A comparison between the simulations by Baalmann et al. (2021) and the Pen et al. (2003) model used in this work shows similar results. Due to the Pen et al. (2003) model excluding the radiative cooling process and being solved on a Cartesian grid, the bow shock width is somewhat different. The study also investigated variations in the relative velocity and ISM magnetic field strength on λ Cephei's astrosphere, where, when the relative velocity was decreased from 80 km/s to 40 km/s. The size of the astrosphere increased, with the largest difference seen in the bow shock regions. The effect of the ISM magnetic field on the astrosphere's form was also investigated. When the ISM magnetic field increased, the structure of the astrosphere changed, and due to the high ISM magnetic field, the astrosphere became asymmetrical.

Keywords: Magnetohydrodynamics; stellar wind; astrosphere; interstellar medium; λ Cephei; termination shock; bow shock.

Table of abbreviations

A table containing a list of abbreviations that will be used throughout the text.

AMF	Astrospheric Magnetic Field
AP	Astropause
BS	Bow Shock
D	Dimension
Gaia	Global Astrometric Interferometer for Astrophysics
HCS	Heliospheric Current Sheet
HD	Hydrodynamic
HMF	Heliospheric Magnetic Field
HP	Heliospheric Pause
HTS	Heliospheric Termination Shock
IAS	Inner Astrosheath
IHS	Inner Heliospheric
IPHAS	INT Photometric Hα Survey of the Northern Galactic Plane
IMF	Interplanetary Magnetic Field
ISM	Interstellar Medium
LBV	Luminous Blue Stars
LISM	Local Interstellar Medium
MHD	Magnetohydrodynamic
MIPS	Multiband Imaging Photometer for Spitzer
OAS	Outer Astrosheath
OHS	Outer Heliospheric
SW	Stellar Wind
SNR	Supernova Remnants
TS	Termination Shock

Table 1: *Typical physical constant and non-standard units in centimeter-gram-second units will be used throughout this work (Richardson, 2019).*

Name	Symbol	Value	Units
mass of proton	m_p	1.6726×10^{-24}	g
Boltzmann constant	k_B	1.3807×10^{-16}	erg/K
Planck constant	h	6.6261×10^{-27}	erg.s
Astronomical units	1 AU	1.496×10^{13}	cm
Parsec	1 pc	3.086×10^{18}	cm
kilometres per second	1 km/s	10^5	cm/s
Solar radius	$R_\odot$	6.957×10^{10}	cm
Solar luminosity	$L_\odot$	3.828×10^{33}	erg/s
Solar mass	$M_\odot$	1.988×10^{33}	g

Chapter 1

Introduction

An astrosphere is a large-scale structure resulting from the interaction between a star's outward-flowing stellar wind (SW) and the surrounding interstellar medium (ISM). The relative motion of the star, in relation to its local interstellar medium, gives rise to the formation of a bullet-shaped bubble, typically characterised by supersonic outflow and relative speeds. These give rise to the formation of a termination shock (TS) and a bow shock (BS), respectively.

The termination shock (TS) is the transition from supersonic to subsonic speeds for the SW. The astropause (AP) serves as the discontinuity between the SW outflow and the flow of ISM, effectively separating the two fluids. The bow shock (BS) is located between the AP and the undisturbed ISM. The region situated between the TS and the BS is termed the astrosheath, comprising the inner astrosheath positioned between the TS and the AP and the outer astrosheath extending from the AP to the BS.

Chapter 2 will give an introduction showing that the structure and shape of an astrosphere depend on the type of star. The most well-known example of an astrosphere is the heliosphere. The heliosphere is characterised by four distinct regions that are thermodynamically separated by the termination shock and the heliopause boundary. However, if the Sun's motion relative to the local interstellar medium (LISM) is subsonic, the heliosphere might lack a bow shock and instead have a bow wave. The presence or absence of the heliospheric BS is an ongoing subject of debate, contingent upon the composition of the ISM, see McComas et al. (2012b), Scherer and Fichtner (2014).

Observations of the solar wind speed, density and temperature upstream of the

termination shock and the region close to the heliopause have been observed by Voyager 1 and Voyager 2, also the post-shocked observation in (Richardson et al., 2022), with simulations by Strauss (2013) and others yielding a reasonable approximation to those results. Also, the solar magnetic field is frozen in the solar wind and transported by the solar wind into interplanetary space. This magnetic field is known as the heliospheric magnetic field or interplanetary magnetic field, first described by Parker (1958).

The structure of an astrosphere is modelled using various hydrodynamic (HD) and magnetohydrodynamic (MHD) models. These models include the two-dimensional model by Fahr and Kausch (2000), Scherer and Ferreira (2005), Ferreira and de Jager (2008), the three-dimensional magnetohydrodynamic (MHD) model discussed in Pen et al. (2003), and the three-dimensional magnetohydrodynamic model by Kissmann et al. (2018) called the Cronos model. Apart from solving the standard MHD equations, these models may include or exclude radiative cooling, see Chapter 3.

This study will investigate some of the parameters that influence the evolution of the astrospheric structure using the two-dimensional model discussed above. These parameters include the simulation time, mass loss rate, ISM density, ISM magnetic field, ISM temperature, and stellar wind (SW) outflow speed, see Chapter 4. The compression ratio, the bow shock width, and the radius of the bow shock will be calculated and shown as a function of simulation time.

The astrospheric structure of λ Cephei is studied in Chapter 5. Observational images discussed in Baalmann et al. (2020) and the three-dimensional magnetohydrodynamic model simulation from Baalmann et al. (2021) of λ Cephei will be shown to show the TS, AP and BS. The three-dimensional magnetohydrodynamic model results from Baalmann et al. (2021) are compared with that of the Pen et al. (2003) model. The influence of the relative velocity and the impact of the ISM magnetic field strength on the astrosphere of λ Cephei, using the Pen et al. (2003) model, will shown.

Chapter 2

Astrosphere

This chapter introduces the reader to the astrospheric structure and also discusses its evolution in different interstellar conditions. An astrosphere's evolution depends on various factors, such as its mass, age, and activity. In addition, the density and temperature of the surrounding interstellar medium play an important role in determining the astrospheric structure. This chapter will briefly discuss these. One of the most important examples of an astrosphere is the heliosphere. Analysing heliospheric observations and theoretical insights can provide valuable insights into astrospheric structures.

2.1 Star formation

An astrosphere's structure and shape depend on the type of star. Generally, stars are classified based on distinct spectral characteristics (Russell, 1914). The most common system used to differentiate stars from the hottest to the coolest is the Morgan-Keenan system (Morgan and Keenan, 1973), shown in Table 2.1. The Morgan-Keenan system uses the letters O, B, A, F, G, K, and M, with the hottest being O and the coolest being M.

Stars are formed in interstellar gas clouds that are dense, cool, and collapse under critical pressure. After young protostellar systems are formed, the complex interplay of various physical processes within molecular clouds, such as turbulence, conservation of angular momentum, gravitational interactions, and magnetic fields. The effects of stellar feedback can lead to relative motion among these young protostellar systems and ultimately lead to the transition from their dense birthplaces.

Table 2.1: *The Morgan Keenan classification system using the Hertzsprung-Russell diagram (Chaisson et al., 2005).*

Class	Chromaticity	Temperature (Kelvin)
O	Blue	30000
B	Blue - white	10000 - 30000
A	white	7500 - 10000
F	Yellow- White	6000 - 7500
G	Yellow	5200 - 6000
K	Light orange	3700 - 5200
M	Orange - red	2400 - 3700

Young protostellar systems can transition from a frigid and dense interstellar gas environment to a hotter and less compact interstellar gas environment surrounded by dense clouds. Moreover, they undergo significant environmental changes after some period and exhibit more consistent but less intense winds when, for example, entering the T-Tauring stage[1] (Hartmann, 2009). These winds can be of wave-like characteristics, such as solar wind or dust-driven type or of the radiation-pressure like of the winds emanating from bright O and B stars, Cassinelli and Lamers (1987), Dupree and Reimers (1987) and Holzer (1989).

Furthermore, wind-driven stars, such as O and B stars, are characterised not only by their high mass loss rates ($\dot{M}_S = d(M_S)/dt$) but also by the specific momentum loss, which relates to how mass and energy ejected from the star. The mass loss rate is the rate at which a star loses mass over time. The specific mass loss rate and the specific momentum loss influence the formation of an astropause (AP) as plasma from the star and the local interstellar medium move in different directions (Weaver et al., 1977). Therefore, the duration of the adaptation period (the period before the formation of an astropause) varies among different types of stars. For T-Tauri stars and Wolf-Rayet stars (massive evolved stars that have lost their outer hydrogen envelopes, exposing their hot and helium-rich cores, Crowther, 2007), the adaptation period is comparatively lengthy, lasting at least 10 000 years. On the contrary, lower-mass stars like G-type stars, including the Sun, have less intense mass loss and shorter adaptation periods (around 300 years). The previously mentioned indicates that the formation of an astropause occurs relatively quickly in G stars (Fahr and Scherer, 1995).

Moreover, when a star moves relative to its local interstellar gas environment, an astrospheric bubble is formed, such as runaway stars, stars ejected from their original

[1] T-Tauring stage is the process in which young pre-main-sequence stars are still in the process of forming, known as T-Tauri stars (Hartmann, 2009).

stellar groups, or binary star systems at very high velocities. These stars typically move at fast speeds between 40 km/s to 200 km/s relative to their local environment Blaauw (1961), Gies (1987), Hoogerwerf et al. (2001) and Perets and Šubr (2012). Due to this, a bow shock forms as they move through their local interstellar environment at supersonic speeds. The interstellar medium is swept up in front, forming the bow shock. In contrast, stars that move at subsonic speeds show a bow wave instead of a bow shock (McComas et al., 2012a).

It is possible for magnetic pressure, kinetic ram pressure (associated with the motion of the plasma), and thermal pressure (related to the temperature of the plasma) to influence the geometrical shape of these astrospheric boundaries, Fahr and Neutsch (1983), Frisch (1993) and Fahr et al. (1986) for more details.

2.2 Heliospheric physics

One of the most well-known examples of an astrosphere is the heliosphere. The heliosphere is formed by the interaction between the solar wind and the surrounding interstellar medium, as described by Parker (1963). Since then, it has been the subject of much research and study. This section will explore some background knowledge regarding the formation of heliospherc structures, which gives a good understanding of what is expected of other astrospheres.

2.2.1 The Sun

The Sun is a yellow dwarf star and is the closest star to Earth. The mass of the Sun consists of 90% hydrogen, 10% helium, and trace amounts of components like carbon, nitrogen, and oxygen, which total approximately 1% (Kivelson et al., 1995). The structure of the Sun has six different regions, mainly the corona, chromosphere, photosphere, convection zone, radiative zone, and core. The solar interior comprises the core, radiative, and convection zones, with the remainder belonging to the atmosphere and solar surface. The interior of the Sun is unobservable. Our knowledge of the structure of the solar interior is, therefore, based on theoretical solar models, Kivelson et al. (1995) and Hoogerwerf et al. (2001).

The Sun exhibits an 11-year periodicity known as the solar cycle. The hypothesis of this cycle results from interactions between the Sun's internal dynamo, magnetic

fields, and the differential rotation occurring within the Sun. This cycle involves variations in solar activity, including changes in the number of sunspots, solar flares, and the solar magnetic field (Usoskin, 2008). Sunspots are dark, cooler regions on the Sun's surface (Babcock, 1961), and are associated with concentrated magnetic fields that inhibit convection, leading to reduced surface temperatures. Sunspots often appear in pairs, with each spot having a magnetic polarity opposite its partner. These magnetic pairs are a vital feature of sunspot groups, Solanki (2003) and Moore and Rabin (1985).

Moreover, because the sunspot group includes a bipolar magnetic region, an active region[2] (AR) is formed Muñoz-Jaramillo et al. (2021) and McClintock et al. (2014). The presence and behaviour of sunspots, including their magnetic polarities, are described by Hale (1908). These laws state that sunspots within a given hemisphere of the Sun have the same magnetic polarity during one solar cycle and the opposite polarity during the next cycle. Hale's laws provide insight into the Sun's magnetic reversals over time. Sunspot groups can vary in size and complexity. Each isolated group may contain one or multiple individual sunspots, and their sizes can range from 10 square degrees or more (Temmer et al., 2006).

The solar cycle is monitored by counting the number of sunspots on the Sun's surface. Figure 2.1 displays the yearly and monthly relative sunspot numbers averaged from 1944 to 2017. These numbers serve as an activity index that quantifies the level of solar activity. The solar cycle exhibits two primary phases: solar minimum and solar maximum. During a solar minimum, the Sun is relatively less active, and the number of sunspots is typically small; in contrast, during a solar maximum, the Sun is more active, and the number of sunspots is greater (Norton et al., 2023).

2.2.2 Solar wind

The solar wind is a continuous stream of charged particles, or plasma, originating from the Sun's outermost atmosphere, the corona. This plasma is heated to high temperatures within the corona. When it reaches a point where the Sun's gravitational pull can no longer contain it, it is expelled into space, creating the solar wind. The plasma in the solar wind follows the Sun's magnetic field lines, which extend radially outward from the Sun's surface. Due to its plasmatic nature, the solar wind carries the Sun's magnetic field as it flows outward into space (Biermann, 1957).

[2]Active region is a region on the solar surface where there is a higher level of magnetic activity compared to the surrounding areas

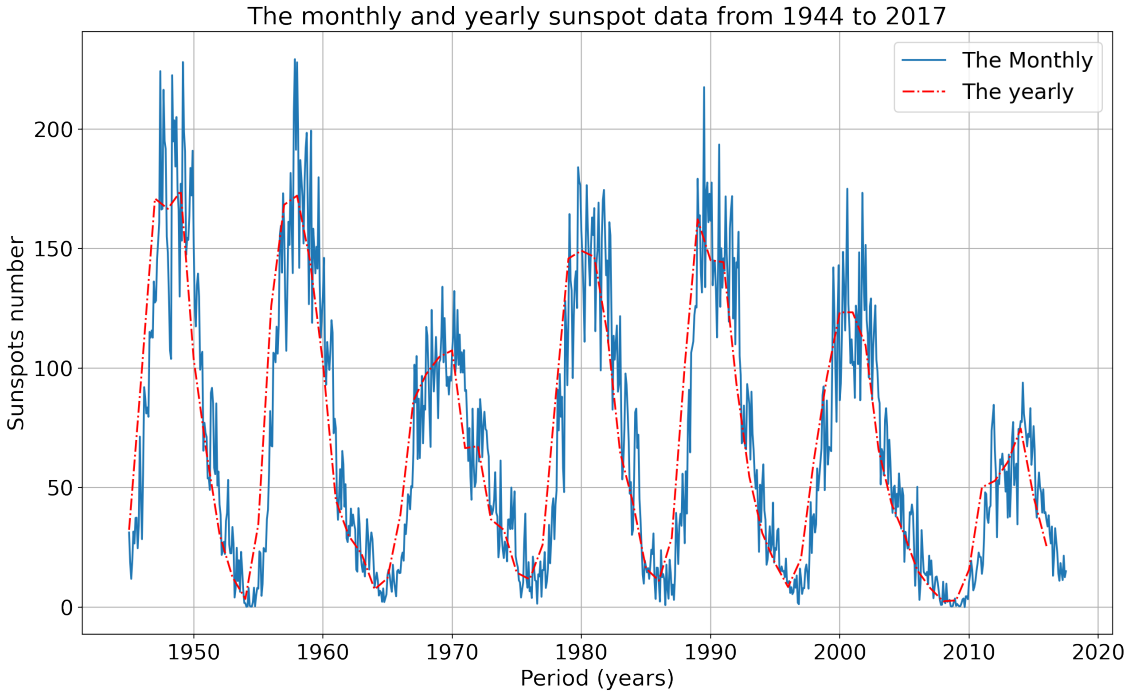

Figure 2.1: *The number of sunspots from 1944 to 2017. The blue line shows the monthly data, while the red dash-dot line represents the yearly data. Data from:* https://ngdc.noaa.gov/stp/space-weather/solar-data/solar-indices/sunspot-numbers/american/lists/ .

The Sun experiences differential rotation, meaning that different parts of the Sun's surface rotate at different speeds because the Sun is not a solid body but is composed of hot, ionised gas (plasma), and its rotation is not uniform throughout (Beck, 2000). The factors that contribute to this differential rotation are as follows:

- The Sun's interior is not well-mixed. The transition region between the radiative zone and the convective zone is called the tachocline. The tachocline is presumed to be the region where the Sun's differential rotation is generated. It is a layer where the Sun's magnetic field is generated and shaped, and it plays a critical role in the Sun's rotation dynamics, Balbus and Latter (2010) and Miesch et al. (2006).

- The Sun's magnetic field lines are generated by the motion of charged particles (mainly protons and electrons) in its outer layers. These charged particles are affected by the Sun's magnetic field, which in turn is influenced by the differential rotation. As a result, the Sun's magnetic field lines become twisted and stretched due to the differential rotation (Moss, 1992).

As a result of these factors, the Sun's equatorial regions rotate faster than the

polar regions. This differential rotation can cause the Sun's magnetic field lines to become twisted and form a spiral pattern above the Sun's polar regions. Over time, the magnetic field lines can become buoyant and rise to the surface, leading to sunspots, solar flares, and coronal mass ejections (Solanki, 2007).

There are regions within the corona where the magnetic field lines are open or have "gaps." These gaps create corridors for the plasma to escape from the Sun's gravitational pull. These regions are often associated with coronal holes, which are lower in temperature and less dense areas in the corona. Within these open magnetic field line regions, the high-temperature plasma is ineffectively contained by the magnetic field. Instead, it follows the path of least resistance and streams outwards into space. This escaping plasma, composed of charged particles (primarily electrons and protons), is guided by the magnetic field lines and is released into space as the solar wind, Solanki (2003) and Aschwanden (2006).

The Sun's magnetic field and the differential rotation of the Sun, play an important roles in shaping and controlling the solar wind. Still, the initial source of the solar wind is the hot and highly energetic corona, Schwenn (1983), Withbroe et al. (1991), Scherer et al. (2000) and Cranmer and Winebarger (2019).

Characteristics of the solar wind

In 1990, the Ulysses spacecraft was launched to make observations of the equatorial and polar regions close to the Sun by completing multiple orbits around the Sun. This was done by passing over the Sun's south and north poles and measuring the solar wind speed, magnetic field strength, direction and composition (Smith and Marsden, 1995). Some of the observations from the spacecraft are shown in Figure 2.2. In Figure 2.2, panel (a) shows the Ulysses heliographic latitude in degrees with the heliocentric distance in astronomical units showing the spacecraft's position, including the three fast latitude scans. Panel (b) shows the observed solar wind plasma speed, and panel (c) shows the magnitude of the interplanetary magnetic field (IMF) or heliospheric magnetic field (HMF). Ulysses made three latitude scans, as shown in the green writing. The first and third were in a period with minimal solar activity, and the second was in high solar activity. During these fast latitudinal scans, the Ulysses spacecraft was between $\sim$ 1.3 AU to $\sim$3 AU away from the Sun.

During solar minimum periods, at latitudes of -35^o to 35^o (near and within the Sun's equator at mid-latitude), the solar wind showed that the lowest average speed was

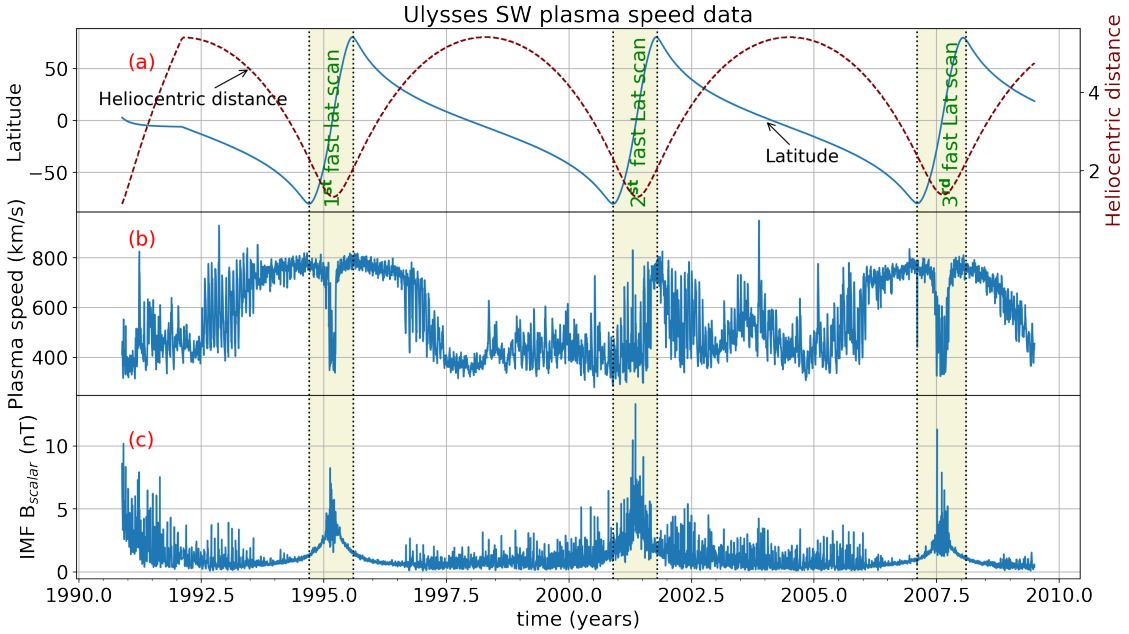

Figure 2.2: *The Ulysses spacecraft showing the latitude and heliocentric distance in panel (a), the solar wind plasma speed in panel (b), and the interplanetary magnetic field or heliospheric magnetic field in panel (c) from 1991 to 2007. Data from:* https://omniweb.gsfc.nasa.gov/coho/.

approximately 315 km/s. This was due to the enclosed magnetic loops and endpoints at the solar surface at lower latitudes. The closed loops emanating from the Sun lead to the formation of streamer belts. The streamer belts exhibit a perpendicular orientation concerning the solar wind's outflow, impeding its escape. Hence, the emergence of the slow solar wind emanates from diminutive coronal holes and the peripheries of more extensive coronal holes, Ofman (2004), Schwenn (2006) and Wang (2012).

In the polar regions, however, the observed solar wind speed was faster, approximately 800 km/s, due to unobstructed field lines with a single end connected to the Sun's surface extending from coronal holes to the vast expanse of interstellar space. These field lines facilitate the radial outflow and development of the fast solar wind, Cranmer (2002) and Huang et al. (2017).

Furthermore, in the 1970s, when Skylab was in operation, it became abundantly clear that the coronal source of the high-speed streams was the area with less brightness at extreme ultraviolet (EUV) and soft X-ray wavelengths. This was called a coronal hole (the regions where the magnetic field lines of the corona are exposed to interplanetary space), demonstrating that the number of electrons and the temperature are much lower in this area, Krieger et al. (1973) and Neupert and Pizzo

(1974).

Also, Phillips et al. (1995) found that the heliosphere structure could be stretched in the polar direction because the wind's outward pressure is more significant over the poles than around the equator. Figure 2.3 shows the schematic representation of the origin of the solar wind at different latitudes with the Sun projection, polar coronal hole projection, active region projection and slow and fast winds.

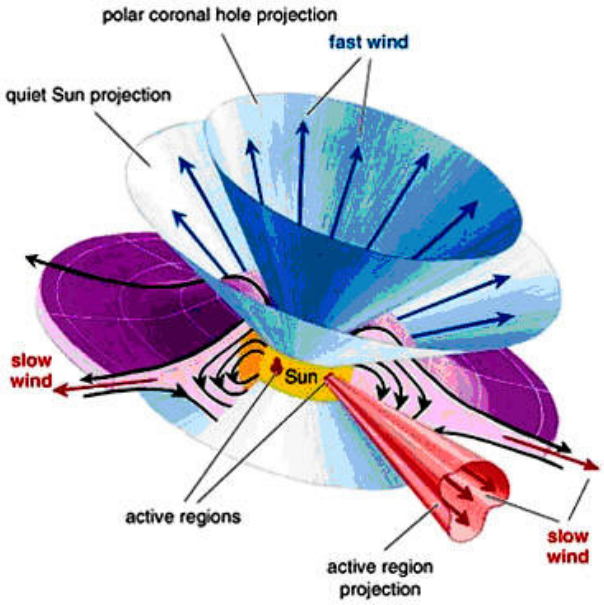

Figure 2.3: *The origin of fast and slow solar wind. Image credit:* https://skyfallmeteorites.com/education-research/glossary/solar-wind/.

An analytical expression can be constructed for the solar wind speed (V), Hattingh (1998), Langner and Potgieter (2004) and Strauss and Potgieter (2010). These authors have included a dependence on both latitude and radial distance in the flow speed expression of the solar wind. It is, therefore, postulated that the radial and latitudinal variables are independent of each other and are given as follows:

$$V(r,\theta) = V(r,\theta)\mathbf{e_r} = V_r(r)V_\theta(\theta)\mathbf{e_r}. \tag{2.1}$$

As discussed in Hattingh (1998), the polar angle measured from the Sun's north pole is θ, the radial distance in AU is r, and $\mathbf{e}_r$ is the unit vector in the radial direction, Langner et al. (2006) and Scherer et al. (2011). The latitudinal dependence $V_\theta(\theta)$ given by Hattingh (1998) for low solar activity is assumed to be given as:

$$V_\theta(\theta) = 1.5 \mp 0.5 \tanh\left(\frac{2\pi}{45}(\theta - 90^\circ \pm \varphi)\right). \tag{2.2}$$

There is no latitudinal dependence for the solar maxima, and it is assumed that:

$$V_\theta(\theta) = 1.0. \tag{2.3}$$

Figure 2.4 illustrates the observed solar wind speeds latitude dependence given by equations 2.2 (representing solar minima) and 2.3 (representing solar maxima). For the model, the northern hemisphere is from $0° \leq \theta \leq 90°$ and the southern hemisphere is from $90° \leq \theta \leq 180°$ with $\varphi = 30°$. Data from the three fast latitude scans of the Ulysses spacecraft are shown and compared to these analytical expressions. There is good agreement, especially for solar minimum periods, as shown.

The radial dependence of the solar wind can be assumed as follows:

$$V_r(r) = V_\circ \left(1 - exp\left[\frac{40}{3}\frac{r_\odot - r}{r_\circ}\right]\right) \tag{2.4}$$

inside the termination shock, in equation 2.4, $V_\circ$ represents the initial solar wind velocity, $r_\circ = 1$ AU is the distance from Earth to the Sun, and $r_\odot = 0.005$ AU is the radial distance at which the solar wind is assumed to be purely radial.

A study conducted by Sheeley et al. (1997) showed that solar wind speed rose from approximately 150 km/s in the vicinity of 5 $R_\odot$ to approximately 300 km/s in the vicinity of 25 $R_\odot$ while using Large Angle and Spectrometric Coronagraph (LASCO) observations. Moreover, Esser et al. (1997) found that the solar speed could reach a value of 750 km/s at a distance of 5 $R_\odot$ with similar results found by Corti et al. (1997). A summary of the average solar wind characteristics associated with two fundamental types of solar wind (slow and fast) at a distance of 1 AU is shown in Table 2.2.

Figure 2.5 shows the radial dependence within the slow and fast solar wind range compared to Voyager 1, Voyager 2, Pioneer 10, and Pioneer 11 data. The model takes the initial speed (V_o) as 250 km/s, 400 km/s and 800 km/s. The light grey area represents the slow speed, and the linen area corresponds to the fast speed.

As shown in Figure 2.5, there are fluctuations between slow and fast solar winds (from 1 AU to 9 AU). However, at radial distances greater than 10 AU, most data indicate a fast solar wind, for the solar wind detected by Pioneer 11 and Voyager 2. The bulk of the data from the various spacecraft falls between 250 km/s to 800 km/s. Additionally, a third form of solar wind arises from coronal mass ejections (CMEs).

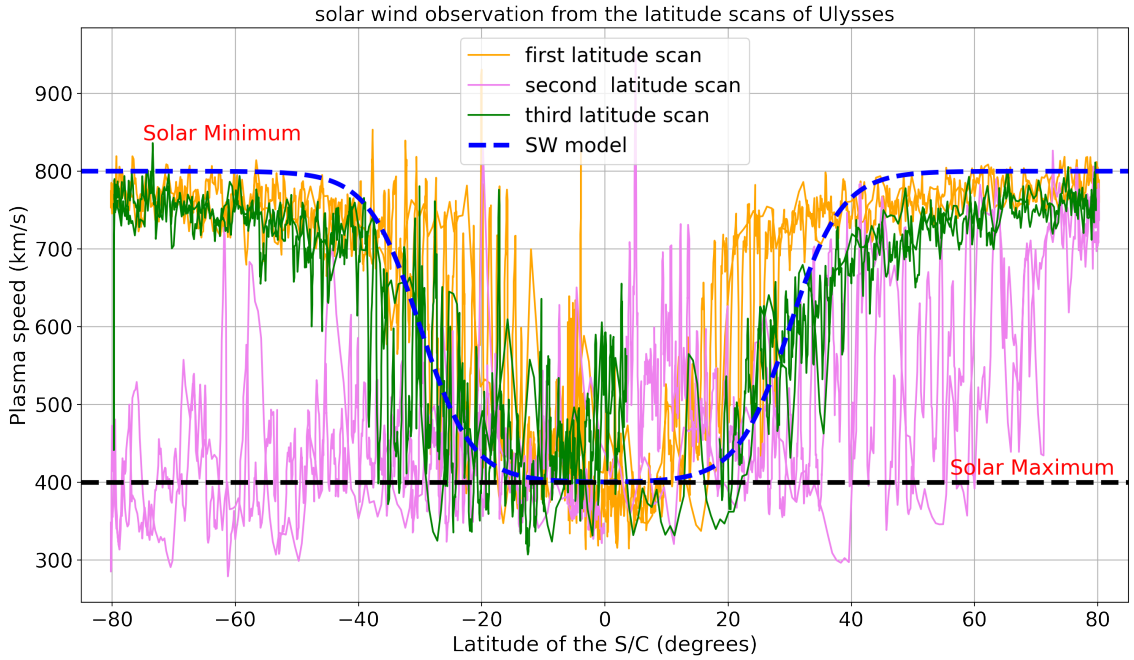

Figure 2.4: *Solar wind speed observed as a function of latitude by the Ulysses spacecraft. The analytical expressions for solar minimum (the blue dash line shows equation 2.2) and maximum (the black line shows the equation 2.3) are shown. The Ulysses data is compared to the model for the three fast latitude scans, with the first latitude scan indicated by an orange line, the second by a pink line, and the final latitude scan, a green line. Data from* `https://omniweb.gsfc.nasa.gov/coho/`.

This kind of solar wind includes a broad spectrum of speeds, between 400 and 2000 km/s, and is frequently associated with interplanetary shocks, Hundhausen (1972) and Schwenn (1986).

Table 2.2: *Typical solar wind parameters at 1 AU during periods of low solar activity (Scherer et al., 2000).*

Parameter	Slow Wind	Fast Wind
Flow Speed	250-400 km/s	400 - 800 km/s
Proton Density	10.7 cm^{-3}	3 cm^{-3}
Proton Flux Density	3.7×10^8 cm^{-2} s^{-1}	2.0×10^8 cm^{-2} s^{-1}
Proton Temperature	3.4×10^4 K	2.3×10^5 K
Electron Temperature	1.3×10^5 K	1.0×10^5 K
Momentum Flux Density	2.12×10^8 dyne.cm^{-2}	2.26×10^8 dyne.cm^{-2}
Total Energy Flux Density	1.55 erg.cm^{-2}.s^{-1}	1.43 erg.cm^{-2}.s^{-1}
Helium Content	2.5 %, variable	3.6 %, stationary
Sources	Streamer Belt	Coronal Holes

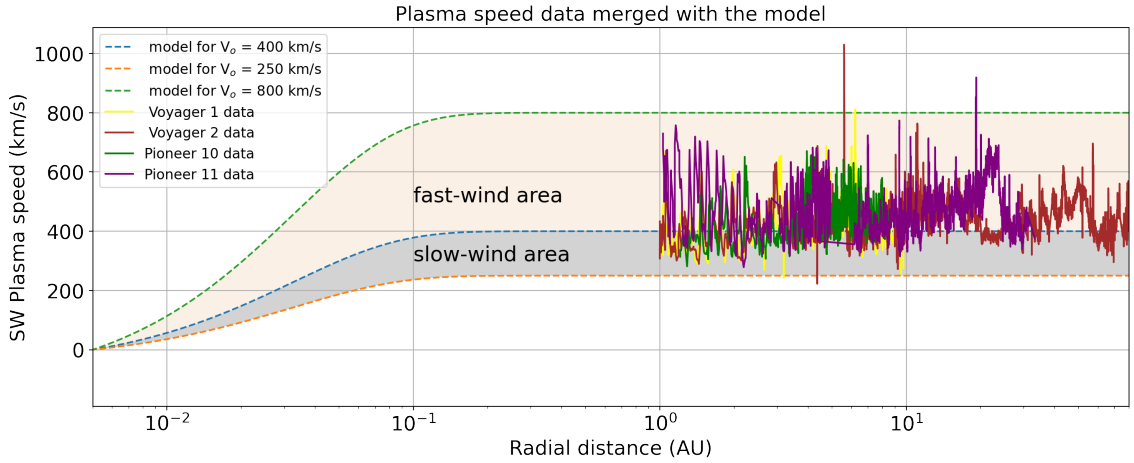

Figure 2.5: *The radial dependence of the solar wind speed inside the termination shock, using Voyager 1, Voyager 2, Pioneer 10, and Pioneer 11 data merged with the model. The line shows the model in equation 2.4. Data from:https://skyfallmeteorites.com/education-research/glossary/solar-wind/.*

2.2.3 Heliospheric magnetic field

The solar magnetic field is entrapped in the solar wind and transported by the solar wind into interplanetary space and is called the heliospheric magnetic field (HMF) or interplanetary magnetic field (IMF). The simplest form was introduced by Parker (1958), referred to as the Parker HMF. In this particular scenario, the rotational movement of the Sun creates the HMF lines to adopt the shape of an Archimedean spiral. These spirals are directed radially outward from the Sun's rest frame and stretch towards interplanetary space. The Parker HMF expression is given as:

$$\mathbf{B} = B_o \left(\frac{r_o}{r}\right)^2 (\mathbf{e_r} - \tan\psi \mathbf{e}_\phi)\,. \tag{2.5}$$

Here, B_o is the heliospheric magnetic field magnitude, $\mathbf{e}_r$ and $\mathbf{e}_\phi$ are unit vectors in the radial and azimuthal directions, and r_o= 1 AU is the distance of Earth from the Sun. The symbol ψ denotes the Parker spiral angle. It determines the winding of the HMF lines and is given as follows:

$$\tan\psi = \frac{\Omega(r - r_\odot)\sin\theta}{V_{SW}}. \tag{2.6}$$

In equation 2.6, V_{SW} represents the solar wind speed; generally ψ is 45^o at the Earth, and when r $\geq$ 10 AU at the equatorial plane, it approaches 90^o. Figure 2.6

shows the HMF for three polar angles, 45^o (orange), 90^o (black) and 135^o (green), for a solar wind speed of 400 km/s. Lately, there have been suggestions for alternative HMF models and their modifications, as proposed by Jokipii and Kota (1989), Moraal (1990), Smith and Bieber (1991) and Giacalone (1999), alongside a range of commonly used HMF models, as discussed by Burger (2005).

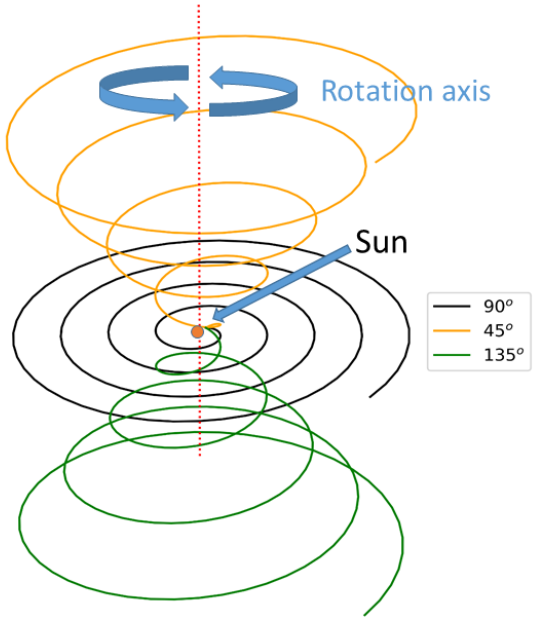

Figure 2.6: *3D structure of Parker field lines (HMF) with the Sun in the centre.*

A study by Wilcox and Ness (1965) noted from magnetic field measurements in space that there is a pattern where the magnetic fields are organised into distinct "sectors", alternating between inward and outward directions. This phenomenon marked the initial identification of what is now known as the heliospheric current sheet (HCS).

According to Smith (2001), the HCS represents the boundary between oppositely directed magnetic field lines, typically originating as extensions of the solar magnetic dipole, and is influenced by factors such as the dipole tilt, solar rotation, and the outward propagation of the solar wind. Peaks and valleys form within the current sheet because of the non-alignment of the rotation and magnetic axes. The HCS extends across the heliosphere, reaching the farthest regions explored by Pioneer and Voyager missions, Burlaga and Ness (1993), Smith (1989) and Smith (1990). It effectively functions as a magnetic equator, with solar wind characteristics, including speed, temperature, density, and composition, varying as a function of distance from the HCS. Notably, the current sheet and sector structure persists throughout the solar cycle, including solar maximum.

At a distance of 1 AU, the width of the HCS measures approximately 10 000 km, while the surrounding plasma sheet is approximately 30 times thicker, as per Smith (2001). Zhou et al. (2005) observed the thickness of the HCS to be finite, decreasing with the radial distance. It's important to note that the magnetic field inside the HCS does not simply diminish to zero and reappear in the opposite polarity. Instead, it undergoes nearly continuous rotations between polarities. Despite theoretical expectations that magnetic fields on opposing sides of the HCS would merge or reconnect, there is limited evidence to support such occurrences (Hoeksema et al., 1983).

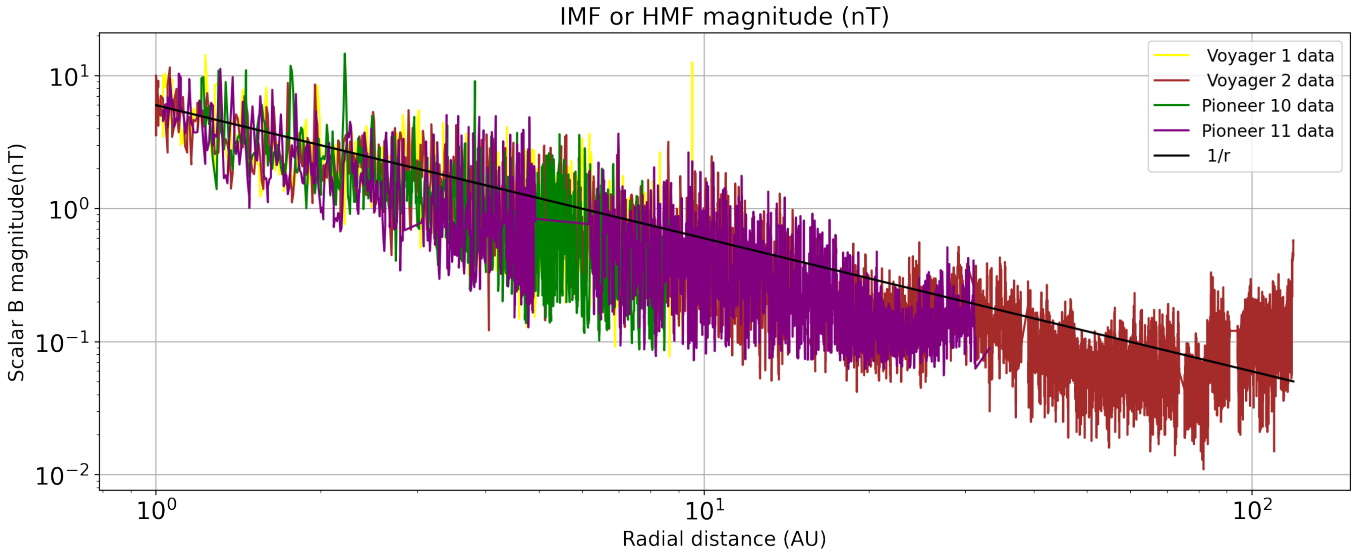

Figure 2.7: *The observed HMF magnitude by the Voyager 1, 2 and Pioneer 10, 11. The black line shows the radial dependency ($\frac{1}{r}$). Data from https://omniweb.gsfc.nasa.gov/coho/.*

Figure 2.2, panel (c), shows that the HMF magnitude at the equator is higher than at the poles, regardless of solar activity levels. This observation suggests that the strength of the heliospheric magnetic field varies with latitude. Radial observations of the HMF were made by spacecraft such as the Voyager 1, Voyager 2, Pioneer 10, and Pioneer 11 and are shown in Figure 2.7. These observations show that the HMF magnitude at 1 AU is higher in relation to further distances from the Sun. The black line shows that the HMF decreased as $\frac{1}{r}$ as the spacecraft moved further from the Sun. As the spacecraft crossed the termination shock at approximately 84 AU, there was a slight increase in the heliospheric magnetic field magnitude. This increase is attributed to the compression of magnetic field lines beyond the termination shock (Zan, 1999). The observations shown in Figures 2.2 and 2.7 show the heliospheric magnetic field variations as a function of latitude and radial distance from the Sun.

2.2.4 Heliospheric structure

Over the past few decades, our understanding of the heliosphere, a vast region of space dominated by the Sun's influence, has advanced significantly. An important moment came in 2004 when NASA's Voyager 1 spacecraft became the first human-made probe to venture beyond the heliospheric termination shock, reaching a staggering distance of approximately 94 AU from our Sun, Stone et al. (2005, 2008) and Decker et al. (2005). The Voyager 2 spacecraft soon followed and crossed the termination shock in August 2007 at a helio-radius of 84 AU, Burlaga et al. (2008) and Stone et al. (2008).

Armed with different scientific instruments, Voyagers 1 and 2 encountered different particle populations in this post-shock region. These particles are neutral atoms, energetic neutral atoms (ENAs), pick-up ions (PUIs), and cosmic rays, each playing vital roles in the dynamic processes that define the heliosphere, particularly in its outer reaches, Scherer et al. (2000) and Zank (2015).

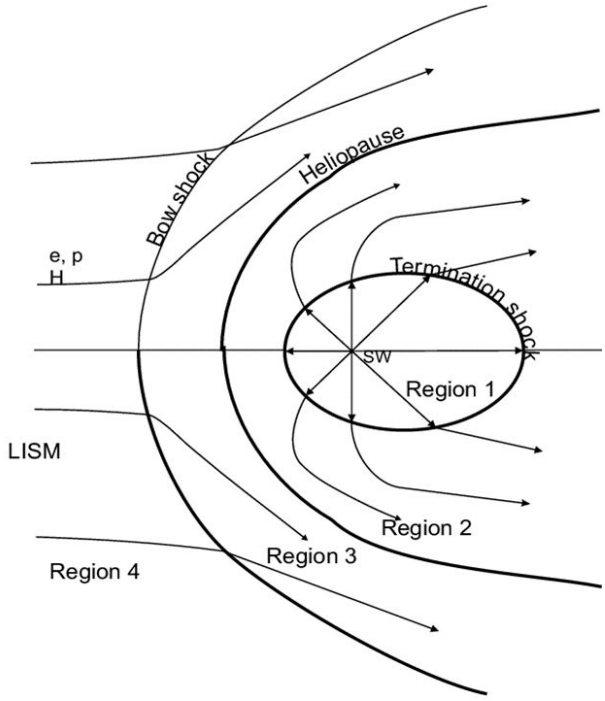

Figure 2.8: *Schematic representation of the heliospheric boundaries. Image from Izmodenov et al. (2003).*

The heliosphere extends over ∼120 AU in the direction of the Sun to the interstellar medium (this direction is toward the nose), and, opposite to this direction, it can extend much further toward the tail. The heliospheric environment, with the surrounding local interstellar medium, can be broken into four distinct thermodynamic regions. The zones illustrated in Figure 2.8 can be described as follows:

- Region 1 is the supersonic wind region, which ends at the heliospheric termination shock (HTS). This zone's conditions are relatively cool temperatures, exceptionally high radial speed (as shown in section 2.2.2), and sparse particle densities.

- Moving outward to Region 2, the inner heliosheath (IHS) is encountered, where the solar wind transforms from its supersonic state to a subsonic through the TS. Here, temperatures rise notably, particle densities increase, magnetic fields intensify, and flow velocities decrease compared to the distant supersonic solar winds to subsonic values.

- Region 3 is the outer heliosheath, the heliospheric pause (HP), a tangential or contact discontinuity and the bow shock (BS). The HP is the border that divides plasma originating from the Sun from plasma that emerged from the interstellar medium. In HP, the density is significantly higher. However, the plasma flow speed is relatively low.

- Region 4 marks the undisturbed ISM plasma. Due to the relative speed of the Sun and the interstellar medium, a bow shock (BS) is found between Region 3 and Region 4 (Zank, 2015).

When the flow speed of the interstellar medium (ISM) falls within the range of 23 to 27 km/s, the presence or absence of the bow shock (BS) becomes an unresolved question. McComas et al. (2012b) and Zieger et al. (2013) demonstrated that the speed of the ISM could dip as low as 23 ± 0.3 km/s and 23.84 ± 0.90 km/s, respectively, resulting in an initial subsonic condition and was enough to argue for the replacement of the BS with the bow wave instead. Conversely, if the interstellar medium begins in a supersonic state, it is possible to hinder the formation of the bow, e.g. due to magnetic pressure within the ISM, see Pogorelov et al. (2009)

An alternative viewpoint posited by Scherer and Fichtner (2014) contends that considering the He^+ component of the local interstellar medium (LISM) results in both Alfvén [3] and fast magnetosonic [4] wave speeds that are lower than the flow speed of

[3] Alfvén waves are waves characterised by transverse magnetic tension, and they propagate along magnetic field lines. These waves can be induced in any electrically conductive fluid that is pervaded by a magnetic field (Finlay, C., 2007).

[4] Fast magnetosonic waves, alternatively referred to as fast MHD waves or fast magnetoacoustic waves, entail compressional movement, leading to alterations in both the magnetic field and plasma density. Their propagation can occur either parallel or obliquely to the magnetic field lines (Chu et al., 2023).

the LISM. Consequently, the established scenario featuring a bow shock preceding the heliosphere remains applicable, as depicted in numerous simulations modelling the interaction between the solar wind and the LISM.

Whether or not a bow shock exists, robust plasma interactions prevent interstellar plasma from blending with the solar wind plasma. This separation is evident in the contact discontinuity, illustrated as the irregular paraboloid heliopause in Figure 2.8, between the HTS and bow shocks (or waves). The heliopause is commonly regarded as the actual boundary of the heliosphere and serves as the boundary line between the solar wind and the ISM plasma. In this work, the astropause would be the boundary of an astrosphere.

Heliospheric observations

Until the early 2000s, what was acknowledged regarding the region beyond the termination shock remained largely theoretical, lacking any observational evidence to validate models that aimed to describe this region. However, a significant turning point occurred when Voyager 1 and 2 traversed the termination shock (TS) and later on transitioned beyond the heliospheric pause (HP). With these two crossings, valuable spacecraft data became available, as shown in Figure 2.9, also see Zank (2015).

This data showed that the solar wind plasma density decreased proportionally to r^{-2} inside the HTS. After the crossing, there was a slight increase in density, coinciding with the deceleration of solar wind speed as it transitioned from supersonic to subsonic at the TS. There was also a notable increase in temperature in the subsonic region, Richardson et al. (2008).

Voyager 1 and 2 spacecraft missions also revealed a notable geometric asymmetry within the heliosphere, with the highest compression occurring in the southern hemisphere, as demonstrated by Opher et al. (2006), who showed that the orientation of the interstellar magnetic field may account for such an asymmetry as shown in Figure 2.10. Also, see Pogorelov et al. (2007), who support these findings. Moreover, models by McComas et al. (2009), Pogorelov et al. (2011) and Heerikhuisen and Pogorelov (2011) strengthened this notion by stating that the tail region of the heliosphere might be deflected upward, further corroborating that the interstellar magnetic field may be inclined.

Strauss (2013) used a 3D MHD model developed by Pen et al. (2003) to calculate

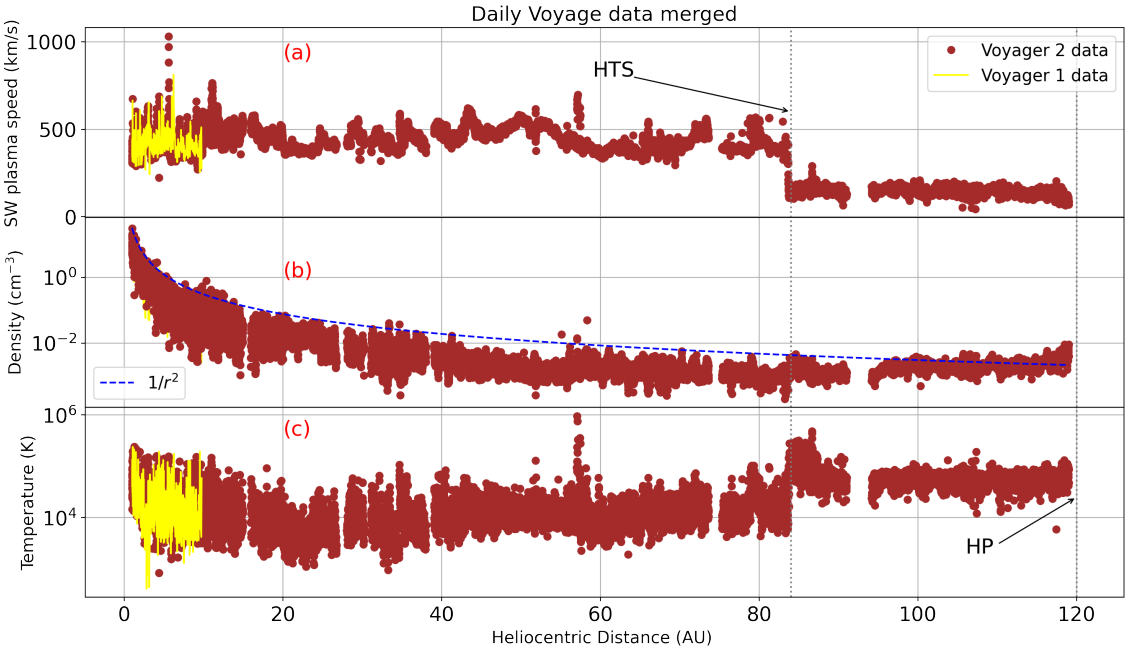

Figure 2.9: *The Voyager 1 and 2 spacecraft daily data as a function of distance. Panel (a) shows the speed of the solar wind, panel (b) presents the density profile, and panel (c) shows the temperature profile. Voyager 1 has crossed the heliospheric termination shock at a heliocentric distance of roughly 94 AU. Data from:* `https://omniweb.gsfc.nasa.gov/coho/`.

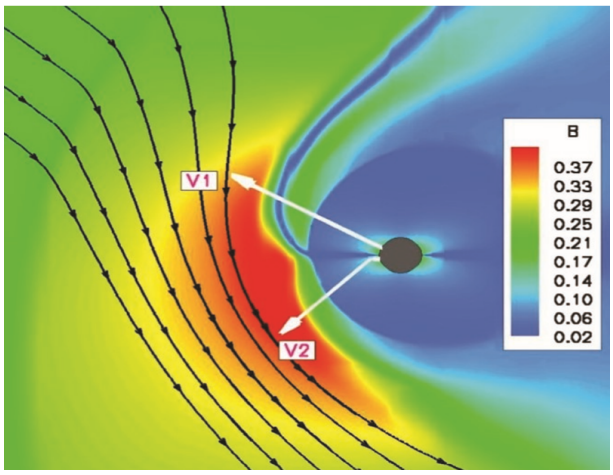

Figure 2.10: *The heliospheric magnetic field strength is shown as a contour plot. The black lines depict the interstellar magnetic field, while the paths of Voyager 1 and Voyager 2 are marked with white arrows. The heliospheric current sheet (shown in deep blue) is bent northward within the heliosheath. Image from Opher et al. (2006).*

different radial profiles, as shown in Figure 2.11. The solid line represents a cross-section along the axis, corresponding to the stagnation line (the symmetry y-axis), and the dashed line corresponds to a cross-section along the z-axis, indicating the north-south direction. The red lines depict the expected dependencies within the pre-shock region.

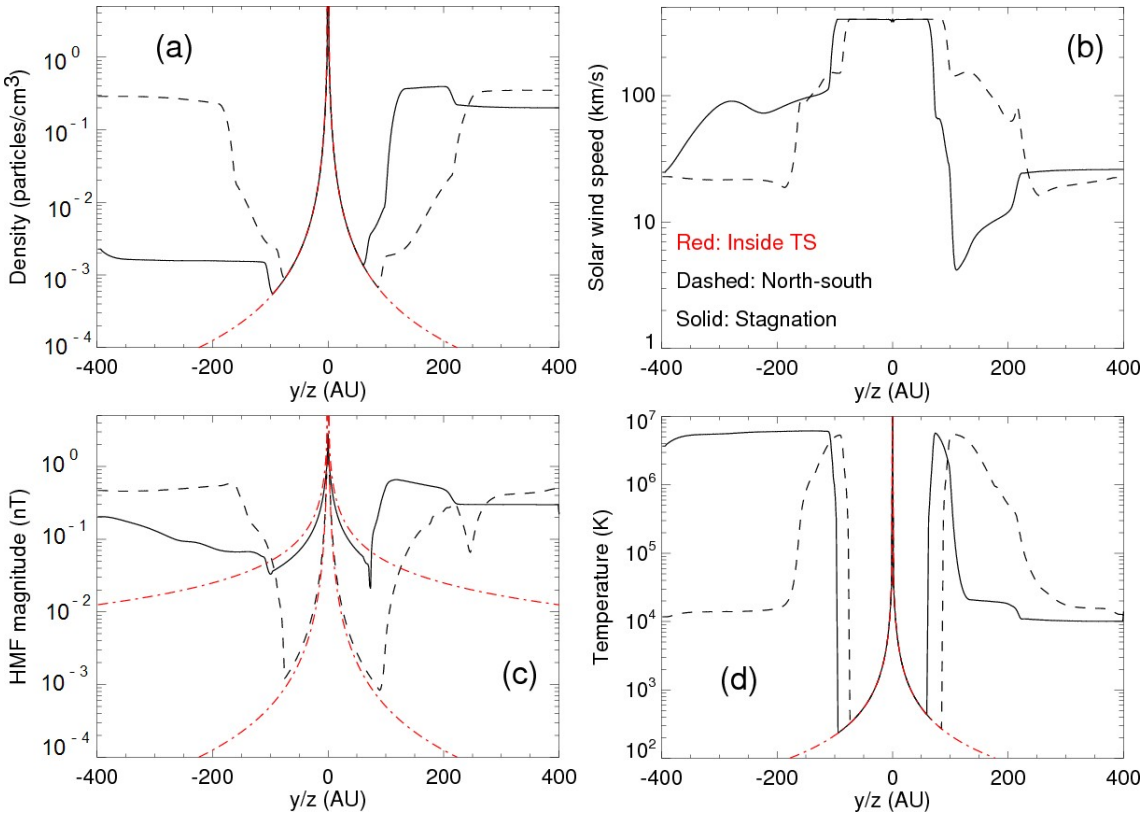

Figure 2.11: *The figure illustrates cross-sections made along two different axes: the y-axis (indicated by the solid line, known as the stagnation line) and the z-axis (represented by the dashed line, termed the north-south line). The red lines depict the expected profiles of these quantities in the supersonic solar wind. Panel (a) displays the density profile, panel (b) shows the solar wind speed, panel (c) shows the magnitude of the heliospheric magnetic field (HMF), and panel (d) shows the temperature distribution. Within panel (c), the presence of two red lines signifies distinct radial profiles of the HMF in both the equatorial and polar regions. Images from Strauss (2013).*

The density profiles in panel (a) exhibit an expected decrease proportional to r^{-2} within the termination shock (TS), followed by a compression of $\sim$4 at the TS. A second compression is evident at the bow shock (BS), primarily observed in the nose direction. The profile illustrates the geometric asymmetry of the TS in the nose direction; the TS is situated at approximately 75 AU, while in the tail region, it extends to around 100 AU, a well-documented nose-tail asymmetry. Similarly, (in the southern hemisphere), the TS is located at approximately 75 AU. In contrast, (in the northern hemisphere) it extends to roughly 100 AU, reflecting the north-south asymmetry initially discovered by the Voyagers spacecraft. The compression of the magnetic field coincides with the solar wind speed change. A more detailed analysis of the heliospheric structure is provided by Zank (2015). Note that the computed density, speed, and magnetic field were in good agreement with the result of the Voyager 2 spacecraft.

Astrospheric structure

Scherer et al. (2015a) discussed a possible and expected astrospheric structure (as shown in Figure 2.12) similar to the heliosphere, as shown in Figure 2.10. The uniform interstellar medium (ISM) originates from the left, and the cylindrical symmetry is due to a single preferential direction aligned with the horizontal axis passing through the star. The key features in this configuration are the termination shock (TS), astropause (AP), and bow shock (BS). Analogous to the heliosphere, the region between TS and BS is the inner astrosheath (IAS), while the region between BS and AP is the outer astrosheath (OAS). IAS is characterised by incompressible and subsonic flow. The AP is a boundary layer that separates the stellar wind from the ISM, marked by a tangential discontinuity with no mass transport. Thermal pressures from the stellar wind and ISM are in equilibrium at the AP's shock front. The BS arises from the astrosphere expanding into the ISM, resulting from supersonic relative motion between the ISM and the star. The existence of a bow shock only requires supersonic relative motion, regardless of whether the star or the ISM exhibits supersonic motion, Scherer et al. (2016a,b).

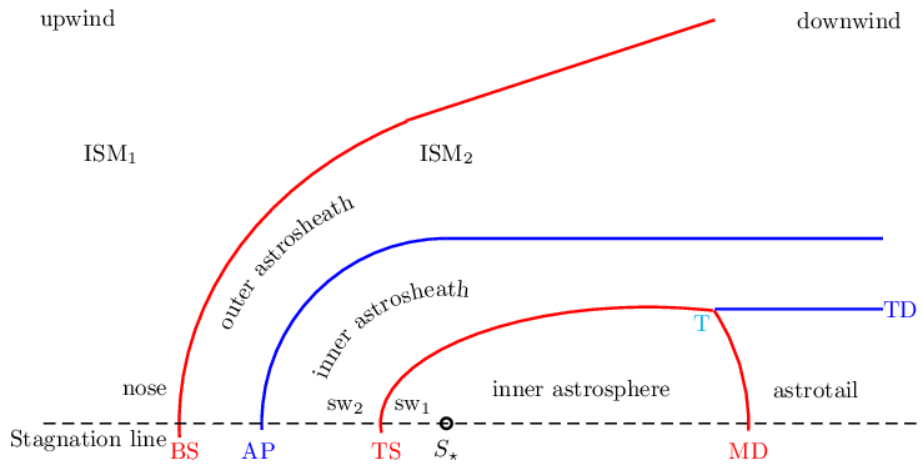

Figure 2.12: *The astrospheric structure schematic for a generic star, showing the TS, AP and BS boundary regions. Image from Scherer et al. (2015a).*

Like the heliosphere, stars possess magnetic fields carried by and integrated into the stellar wind (SW). The SW continuously carries the stellar magnetic field into the astrosphere, creating the astrospheric magnetic field (AMF), Parker (1958) and Owens and Forsyth (2013). In cases where the ISM magnetic field deviates from alignment with the ISM inflow vector, the astrosphere exhibits asymmetry, necessitating a comprehensive 3D magnetohydrodynamic model, as shown by Opher et al. (2006). However, if the ISM magnetic field aligns with the flow vector and the influence of the stellar wind magnetic field is minimal (or both fields are negligible,

as in a hydrodynamical scenario), a simplified 2D axisymmetric model in a single half-plane suffices, as used in chapter 5, see also Baranov and Zaitsev (1995).

2.3 Summary

This chapter briefly discussed some necessary background to understand the intricate structure of an astrosphere. The discussion starts with star formation and various star types, as classified by the Morgan Keenan system. To illustrate the formation of an astropause and bow shock (with particular emphasis on runaway stars), attention was focused on O- and B-type stars, which possess the highest potential for a bow shock due to their elevated relative speeds through the interstellar medium (ISM). Model simulations of such a star are shown in Chapter 5

Furthermore, observations of the main characteristics of the heliosphere, including solar wind plasma speed, the heliospheric magnetic field (HMF), and the interstellar medium (ISM) were examined. As shown, there are three distinct heliospheric regions: the heliospheric termination shock (HTS), the heliospheric pause (HP), and the possible bow shock or bow wave, and, discussed in the context of model and data collected from missions such as Ulysses, Voyager 1, Voyager 2, Pioneer 10 and Pioneer 11, all of which have significantly contributed to the enhancement of our comprehension of the factors influencing the evolution of astrospheric structures.

A schematic representation shown in Figure 2.12 by Scherer et al. (2015a), presented a generic astrosphere and the different boundaries: the termination shock (TS), the astropause (AP), and the bow shock (BS).

Chapter 3

Astrospheric Modelling

3.1 Introduction

This chapter introduces the reader to the astrospheric models used in this work. The models include the two-dimensional model of Fahr and Kausch (2000), Scherer and Ferreira (2005) and Ferreira and de Jager (2008), the three-dimensional magnetohydrodynamic (MHD) model of Pen et al. (2003), and the three-dimensional magnetohydrodynamic model of Kissmann et al. (2018) called the Cronos model. These models use the MHD equations to describe the behaviour of magnetised fluids (plasma) within astrospheres. Choudhuri (1998) and Sébastien (2016) give the MHD equations as follows:

$$\frac{\partial \rho}{\partial t} + \nabla \cdot (\rho \vec{v}) = 0, \tag{3.1}$$

$$\frac{\partial \rho \vec{v}}{\partial t} + \nabla \cdot (\rho \vec{v} \otimes \vec{v} + P^* \mathbf{I} - \frac{1}{4\pi} \vec{B} \otimes \vec{B}) = 0, \tag{3.2}$$

$$\frac{\partial e}{\partial t} + \nabla \cdot [(e + P^*)\vec{v} - \frac{1}{4\pi} \vec{B}(\vec{B} \cdot \vec{v})] = -n_e n_H \Lambda(T), \tag{3.3}$$

$$\frac{\partial \vec{B}}{\partial t} + \nabla \times (\vec{B} \times \vec{v}) = 0, \tag{3.4}$$

$$\nabla \cdot \vec{B} = 0. \tag{3.5}$$

Where the bulk velocity is $\vec{v}$, the density is ρ, the magnetic field is represented by $\vec{B}$, the unit matrix is represented by $\mathbf{I}$, and $\otimes$ is the dyadic product. The pressure is given by $P^* = P + \vec{B}/8\pi$, and the total energy is given by:

$$e = \frac{\rho|\vec{v}^2|}{2} + \frac{P}{\gamma - 1} + \frac{\vec{B}^2}{8\pi}. \tag{3.6}$$

Here γ is the adiabatic index, combined with the induction equation and the restriction that the magnetic field be divergence-free. The equations represent the conservation of mass, momentum, and energy. The pressure expression P^* refers to the ISM's overall pressure, consisting of gas pressure (P) and magnetic pressure ($\vec{B}^2/8\pi$). The radiative cooling is included and given by the expression $-n_e n_H \Lambda(T)$, where n_e is the electron density and n_H is the proton density. The cooling efficiency is given by Λ(T) (Dalgarno and McCray, 1972).

3.2 Two-dimensional MHD model

The first model used in this work will be an extension of the hydrodynamic model by Fahr and Kausch (2000). This model was first applied to calculate the interaction between different fluids in the solar system and the interstellar medium to form a heliosphere. Later, Scherer and Ferreira (2005) used this model to calculate the plasmatic background of the heliospheric environment. From this calculation, the relevant input parameters for a transport model were determined to simulate cosmic ray particles' transport and acceleration within dynamic heliospheric conditions. Also, Ferreira and de Jager (2008) used this model to simulate supernova remnants (SNR) evolution throughout a non-uniform interstellar medium and extended the original hydrodynamic model to include the magnetic field. By doing this, they showed that when the forward shock of a supernova remnant transitions into a medium with a different density, a reflection wave is generated at the interface between the two media and subsequently influences the retention time of the reverse shock of an SNR to the origin shock.

Recently, Light et al. (2022) used this model to simulate the astrospheric structures surrounding luminous blue variable stars (LBV), which are massive O-type stars that show variable outflow parameters and include radiative cooling effects. Their research showed how dynamic changes in the stellar outflow parameters, particularly during eruptions, result in termination shock oscillation. These oscillations, or

eruptions, are then damped in the subsonic post-shock region.

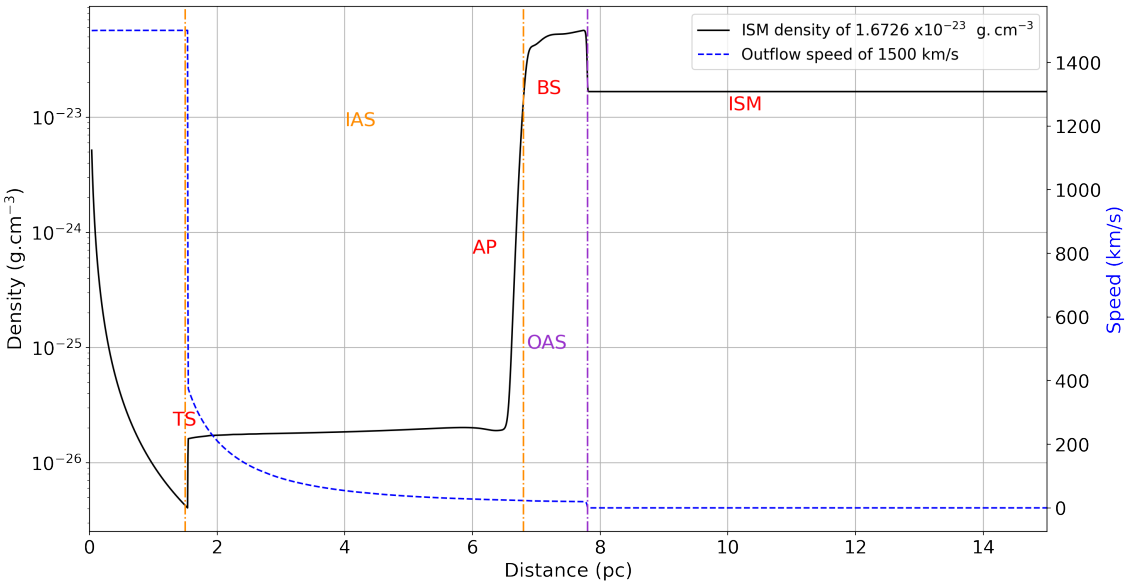

Figure 3.1: *A computed astrospheric density profile after 200000 years of simulation time, using the standard parameters given in Table 3.1. The TS, AP, BS, and the two astrosheath (IAS and OAS) areas are shown.*

Figure 3.1 shows a computed astrospheric structure using the standard parameters given in Table 3.1. The black line represents the computed density profile, and the blue dashed line shows the computed stellar wind outflow speed. The stellar wind density decreases from 5.2× 10^{-24} g.cm^{-3} to 4.1× 10^{-27} g.cm^{-3} from the inner boundary to the termination shock. The location of the TS is at ∼1.54 pc, and the AP is at ∼6.55 pc. The latter is created when the stellar wind ram pressure balances the ISM pressure. At the TS, the density increases (from 4.1× 10^{-27} g.cm^{-3} to 1.8× 10^{-26} g.cm^{-3}), leading to a compression ratio of ∼4, and the stellar wind speed decreases from 1400 km/s to 350 km/s as it decreases from supersonic to subsonic values. The inner astrosheath region is between ∼1.54 pc and ∼6.55 pc. The density increases in the AP until it reaches the outer astrosheath region. The bow shock is located at ∼6.85 PC.

Table 3.1: *Standard parameters assumed in the model.*

Parameters	Standard values
Mass loss rate	2 ×10^{-6} $M_\odot$/year
SW Outflow speed	1500 km/s
ISM density	1.6726 ×10^{-23} g.cm^{-3}
ISM temperature	1000 K
ISM magnetic field	3 μG

The temperature profile of the astrosphere is shown in Figure 3.2 and is calculated from the pressure using the ideal gas law. The parameters are the same as in Figure

3.1. The thermal energy of the plasma decreases up to the termination shock. At the termination shock, the temperature increases as the kinetic energy from stellar matter (stellar wind) is converted to thermal energy, thereby increasing the temperature of the IAS. At the AP, the thermal pressure of the stellar wind and the ISM on opposite sides are equal. Beyond the bow shock, the temperature drops to the interstellar medium temperature.

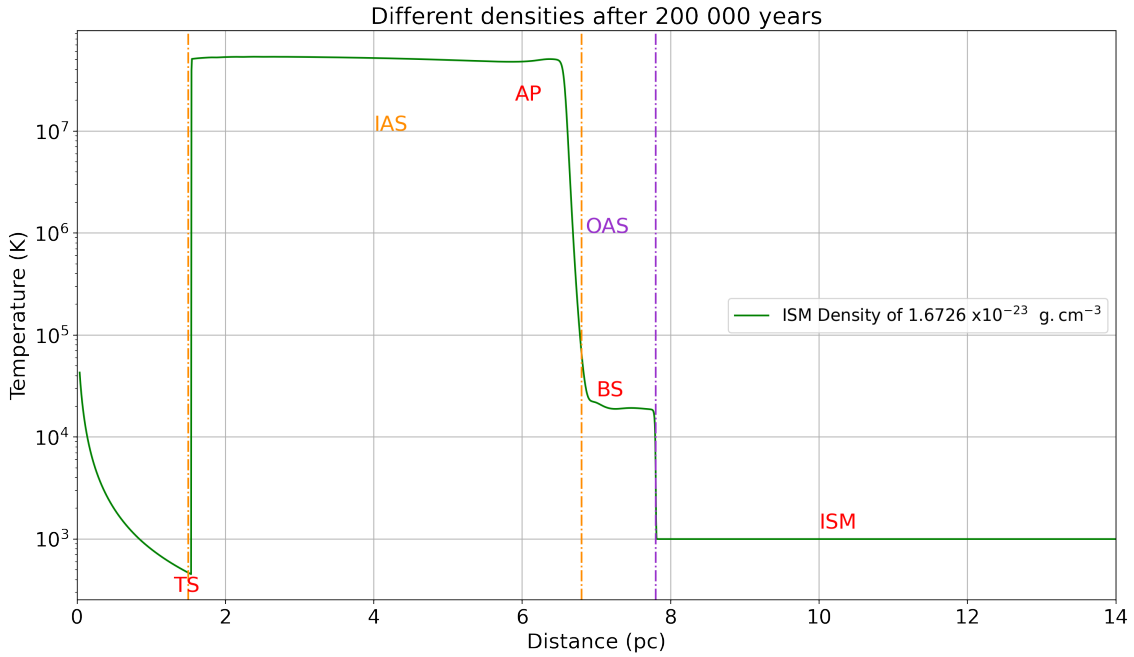

Figure 3.2: *The computed temperature profile after 200000 years of simulation time, assuming the standard parameters given in Table 3.1.*

At the astropause (AP), a state of thermal equilibrium prevails, with the thermal pressures exerted by the stellar wind and the interstellar medium (ISM) on opposing sides achieving equilibrium. Beyond the bow shock, the temperature decreases to that of the surrounding interstellar medium.

3.3 Radiative cooling

This section discusses the effect of radiative cooling on the evolution of an astrospheric structure (Dalgarno and McCray, 1972). Radiative cooling occurs by ionising and exciting atoms, ions and molecules, causing energy loss through radiation emission and is thus dependent upon the gas's composition. Collisional processes transform the thermal kinetic energy of the gas into radiation. Hence, an ion, atom, or molecule will be excited by collisional events and consequently acquire energy until it is emitted as a photon. Furthermore, in this case, a photon can exit the

environment if it is assumed to be optically thin, eliminating the energy obtained and lowering the total thermal kinetic energy of the environment, as discussed in Dyson and Williams (1997). The equation below illustrates how the process occurs:

$$A + B \rightarrow A + B^*,$$

when particle A collides with particle B, causing B to become energised. After a while, this leads to:

$$B^* \rightarrow B + h\upsilon. \tag{3.7}$$

Hence, $h\upsilon$ denotes the energy of the photon released from the collision. Radiative cooling, as mentioned in van Marle and Keppens (2011), is essential for simulations. The addition of radiative cooling in the MHD models leads to a decrease in thermal energy as a result of energy loss due to radiation. As high-thermal-pressure areas cool, the gas transitions from adiabatic to isothermal behaviour. The second effect is the generation of radiative cooling instabilities because the cooling is temperature or density-dependent. If the instability is caused by density-dependent cooling, the high-density zones will lose more energy than the rest of the environment. As a result of the energy loss, the high-density area has a lower temperature, which results in lower local pressure. These areas are compressed due to the decrease in local pressure, increasing the density and thus accelerating the cooling rate, which then repeats the process.

Figure 3.3 illustrates the comparison between two cooling functions proposed by Mellema and Lundqvist (2002) and Schure et al. (2009), showing their temperature dependencies. There are notable differences within the temperature range from 10^4 K to 10^6 K, with the cooling functions differing by a factor of $\sim$2. It is worth noting that the cooling function introduced by Schure et al. (2009) is only defined for temperatures beyond 10^4 K. In contrast, the cooling function proposed by Mellema and Lundqvist (2002) applies to temperatures as low as 10^2 K.

Light et al. (2022) showed the effects of the cooling function of Mellema and Lundqvist (2002) on astrospheric evolution. Figure 3.4 shows the computed density profile after 300000 years of simulation time with the parameters as given in Table 3.2. Including the cooling function in the model increased the bow shock compression ratio during its initial expansion phase. Additionally, it gave rise to the formation of a

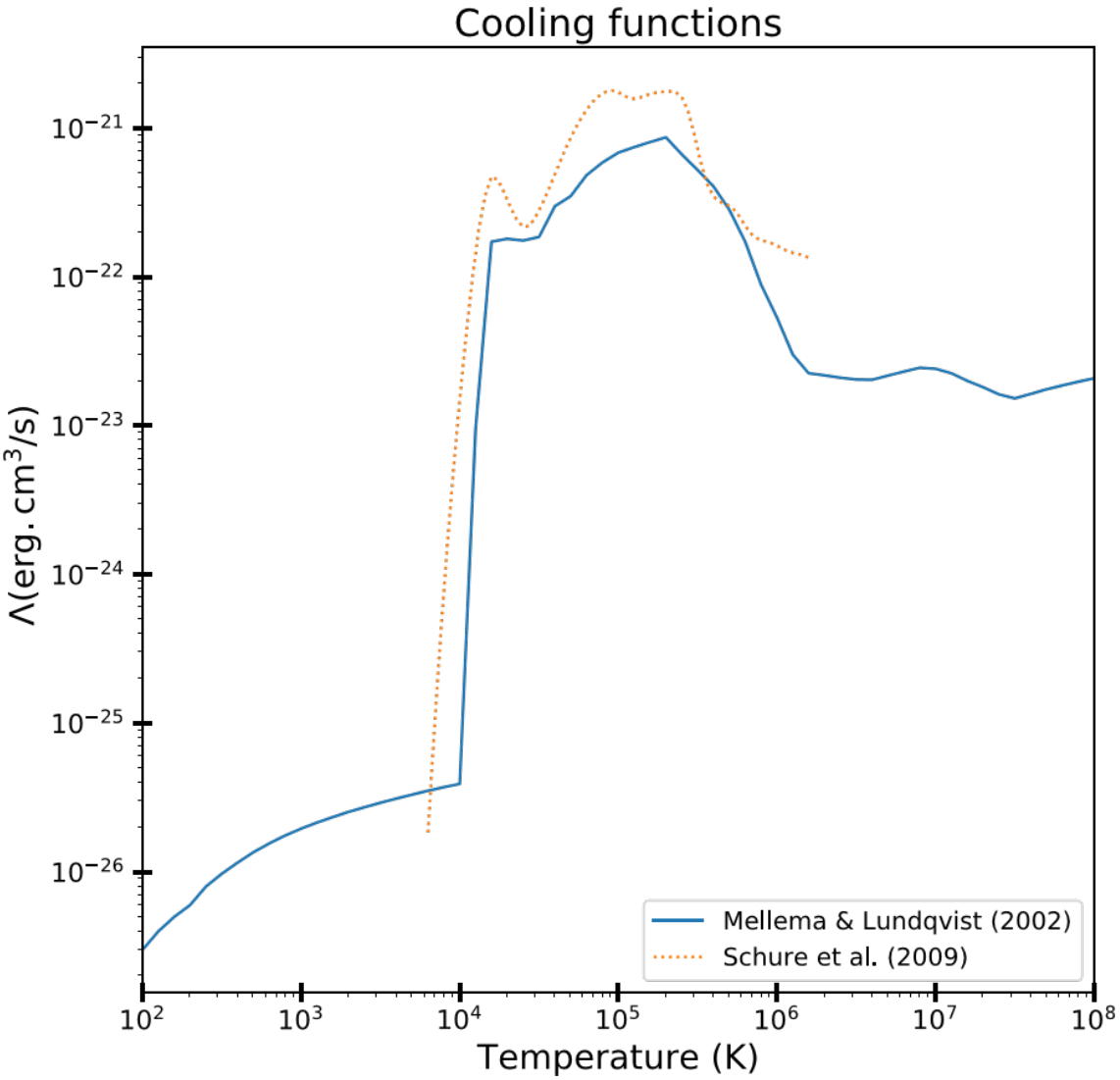

Figure 3.3: *Two cooling functions as a function of temperature. The blue line corresponds to the cooling function of Mellema and Lundqvist (2002), while the dashed orange line represents the cooling function of Schure et al. (2009). Image from Light et al. (2022).*

thin, dense shell in the outer astrosphere. Cooling had a negligible effect within the astrosphere, however, because of the astrosphere's low stellar density, particularly at the termination shock, its impact was proportional to the square of the density. After the cooling had stopped, the thin outer shell expanded once again. The cooling of the thin outer shell resulted in a reduction of thermal pressure, leading to a smaller astrosphere size. Considering the cooling effects, the bow shock moved from approximately 17.7 pc, in the absence of cooling, to roughly 16.8 pc.

It is important to note that other cooling functions exist, including those proposed by Cowie et al. (1981), Sutherland and Dopita (1993), Lykins et al. (2013) and Gnat and Ferland (2012), among others. The cooling function implemented for the 2D MHD model in this study was taken from Mellema and Lundqvist (2002).

Table 3.2: *The parameters used in the Light et al. (2022) simulation.*

Parameters	Standard values
Inner boundary	0.03 pc
Mass loss rate	2.88 $\times 10^{-6}$ $M_{\odot}$/year
stellar wind speed	1000 km/s
ISM density	1 particle.cm^{-3}
ISM temperature	9×10^3 K
ISM magnetic field	3 μG

3.4 The three-dimensional MHD model

The second model used in this study is the 3D MHD model by Pen et al. (2003). Results from this model are shown in Chapter 5. The model solves the MHD equations, utilising a flux-conservative approach, using a second-order total variation diminishing (TVD) scheme, as proposed by Jin and Xin (1995). The MHD equations were solved on a three-dimensional Cartesian grid. The simulation offers several advantages, including high resolution per grid cell, second-order spatial and temporal accuracy, minimal memory requirements, speed, simplicity, and precise enforcement of the $\nabla \cdot \vec{B} = 0$ (Evans and Hawley, 1988).

The model was used by Strauss (2013) to simulate the heliospheric structure. Figure 3.5 (from Strauss (2013)) shows the computed heliosphere in terms of density in panel (a), plasma speed in panel (b), the magnitude of the heliospheric magnetic field in panel (c), and temperature in panel (d) all in the meridian plane of the heliosphere. The Voyager 1 and 2 spacecraft trajectories were also projected onto the same plane. The interstellar flow is directed toward the left. The computed TS were encountered at $\sim$ 80 AU in the equatorial plane. The computed plasma speed shown in panel (b) shows that the solar wind went from supersonic to subsonic. Afterwards, the inner heliosheath temperature increased, as shown in panel (d). The panel also shows a decrease in temperature after passing the heliopause at $\sim$115. A bow shock is also shown at $\sim$ 200 AU. In panel (c), the impact of HMF magnitude also shows the a asymmetry similar to that of Opher et al. (2006). Note the model does not include radiative cooling.

Most recently, the model has been used by Marais (2023) to determine the effects of different grid sizes on the astrospheric simulations. The results are shown in Figure 3.6. These results showed that the profiles became smoother when the grid size increased. For example, in the density profile computed in panel (d), the termination shock and the bow shock for a smaller grid were farther outward and less smooth.

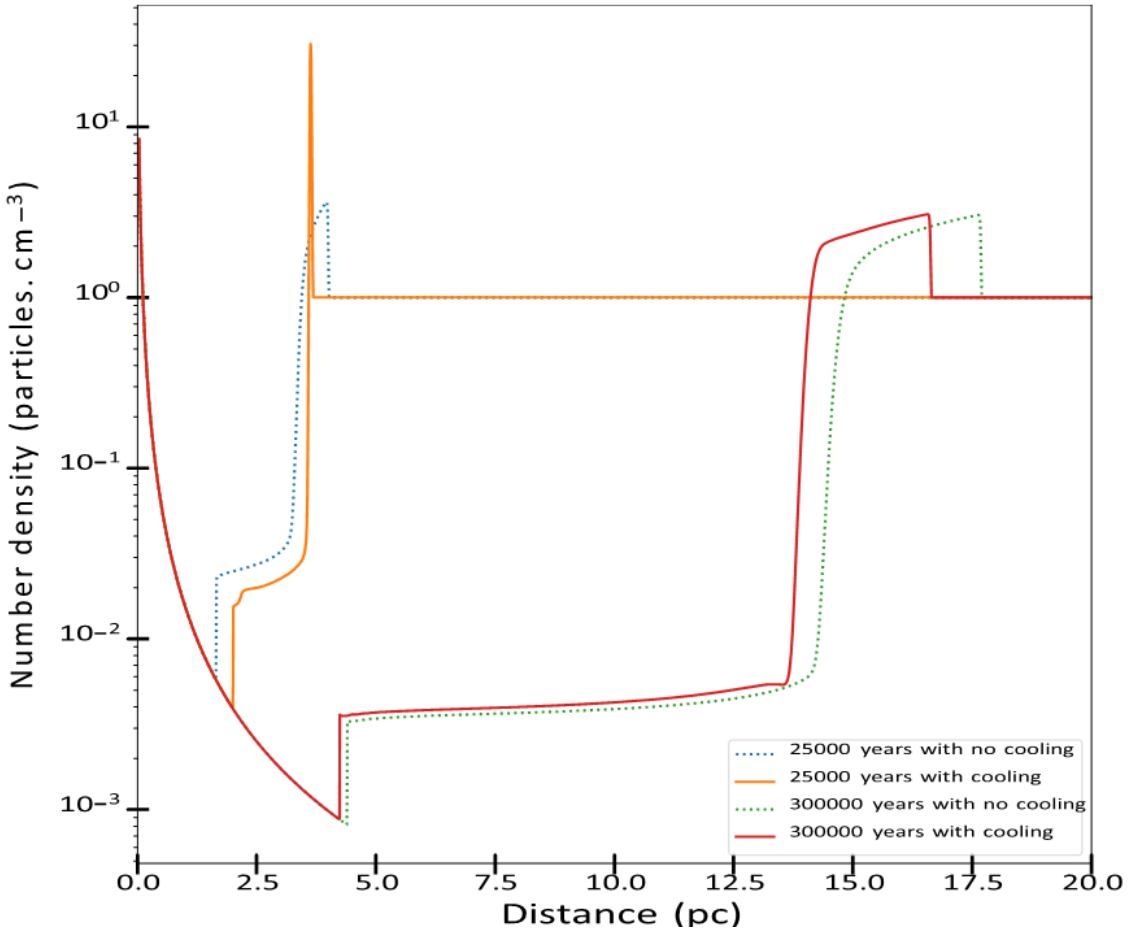

Figure 3.4: *The computed density profile for a pure hydrodynamical case shows the difference between an astrosphere, with and without radiative cooling and also for two different simulation times. Image from Light et al. (2022).*

As a result, the inner and outer astrosheath sizes increased slightly in small grid sizes, with the largest difference occurring in scenarios (a) and (c).

3.5 The Cronos model

In Chapter 5, λ Cephei results from the Pen et al. (2003) model will be shown and compared to those in Baalmann et al. (2020, 2021) who used the Cronos model. The Cronos model was developed by Kissmann et al. (2018) and can solve hydrodynamical and magnetohydrodynamical situations. The model currently supports Cartesian, spherical, and cylindrical coordinates. The model utilises a finite-volume representation and provides various approximate Riemann solvers that are dynamically selected. Note that the current model uses the cooling function of Schure et al. (2009).

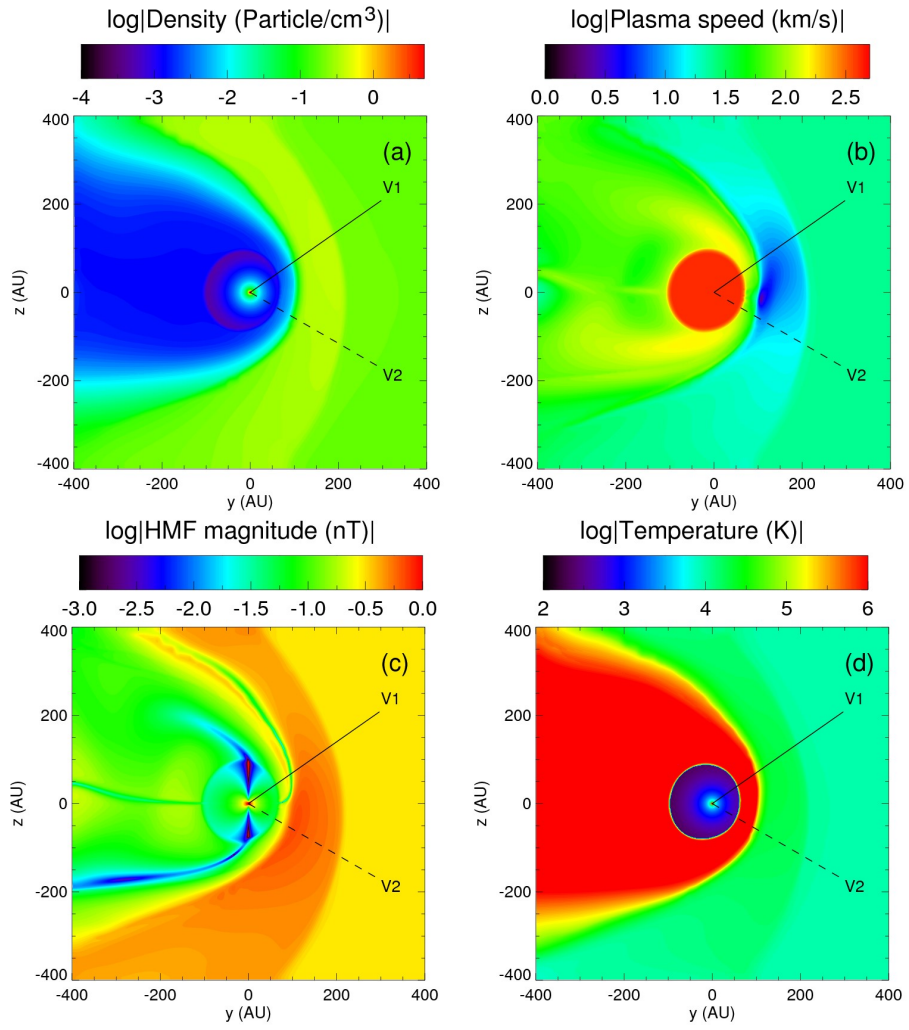

Figure 3.5: *The computed heliospheric environment in terms of density in panel (a), plasma speed in panel (b), HMF magnitude in panel (c), and temperature in panel (d). Images from Strauss (2013).*

Herbst et al. (2020) used the model to study M-stars, focusing explicitly on V374 Peg, Proxima Centauri, and LHS 1140. These particular stars were selected due to their different astrospheric characteristics, aiming to demonstrate that V374 Peg possesses a considerably larger astrosphere than our Sun. In contrast, Proxima Centauri and LHS 1140 likely have astrospheres comparable to or even smaller than our heliosphere, respectively, Herbst et al. (2022) and Scherer et al. (2015b).

In Herbst et al. (2022), the Cronos model was used to simulate the heliospheric structure to assess its suitability for modelling cooler stars. Figure 3.7 illustrates the computed heliospheric densities along the inflow line in panel (a). The figure indicates the termination shock and heliospheric pause as dashed lines. Note that the bow shock was absent around the heliosphere. The absence of a bow shock suggests that the plasma flow speed did not exceed the fast magnetosonic speed, as discussed in Scherer and Fichtner (2014).

Moving to panel (b), the model shows the density profile (in black line) and temperature (in red line) along the stagnation line. Additionally, panel (c) shows the speed (black line) and magnetic field values (red line) as functions of heliospheric distance along the stagnation line. The TS was situated upwind at 92 AU and the HP at 125 AU. The model's results compared to the observations of the Voyager 2 spacecraft were in good agreement. See Chapter 2 and Richardson et al. (2022) for the Voyager 2 spacecraft observation.

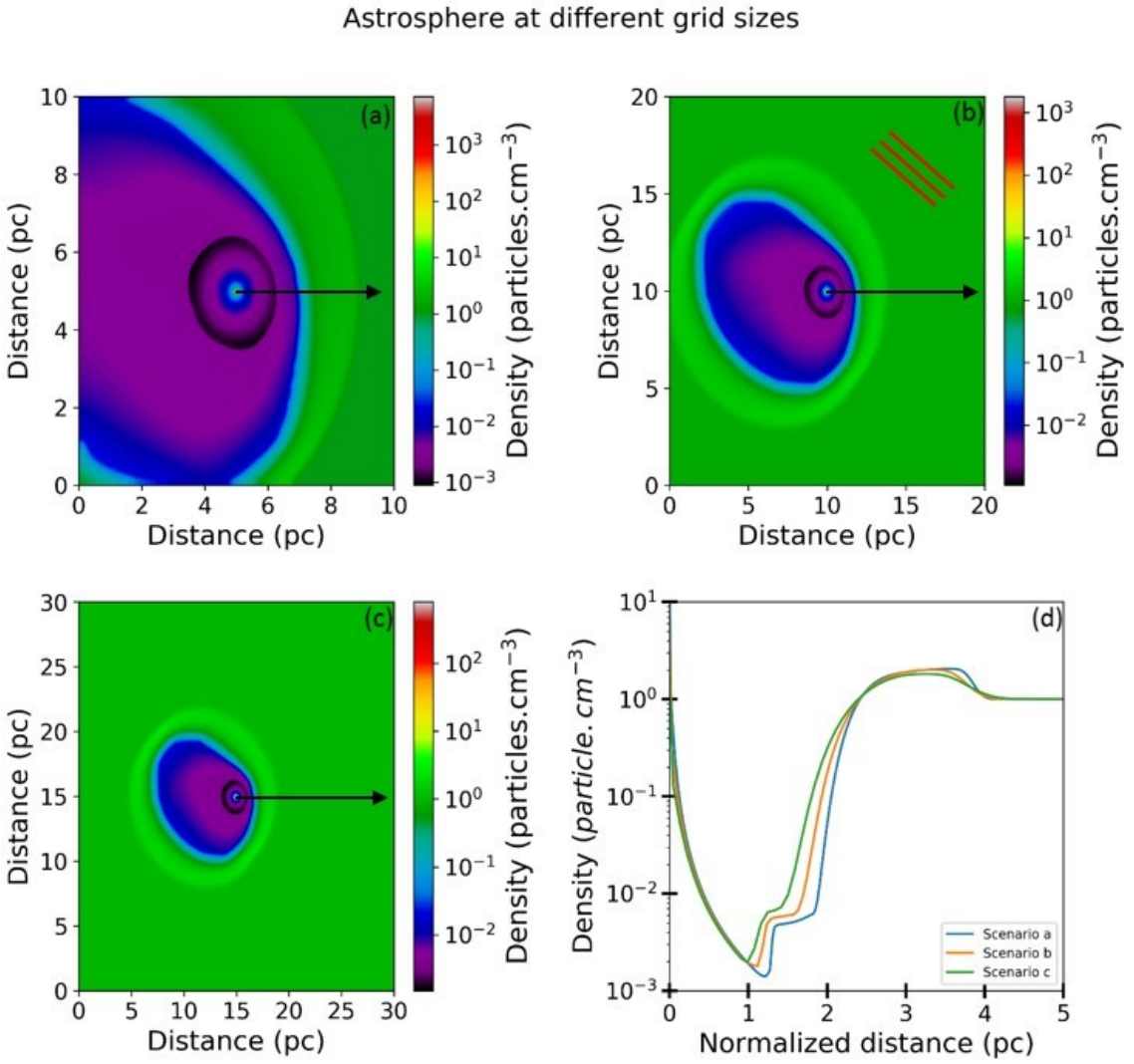

Figure 3.6: *Computed astrosphere for different grid sizes. Scenario (a) has $\triangle x = \triangle y = \triangle z = 10$ pc/350, scenario (b) has $\triangle x = \triangle y = \triangle z = 20$ pc/350, and scenario (c) has $\triangle x = \triangle y = \triangle z = 30$ pc/350. Panel (a) corresponds to scenario (a), panel (b) corresponds to scenario (b), panel (c) corresponds to scenario (c), and panel (d) shows the compared density profiles as a function of radial distance for the different grid size scenarios. Images from Marais (2023).*

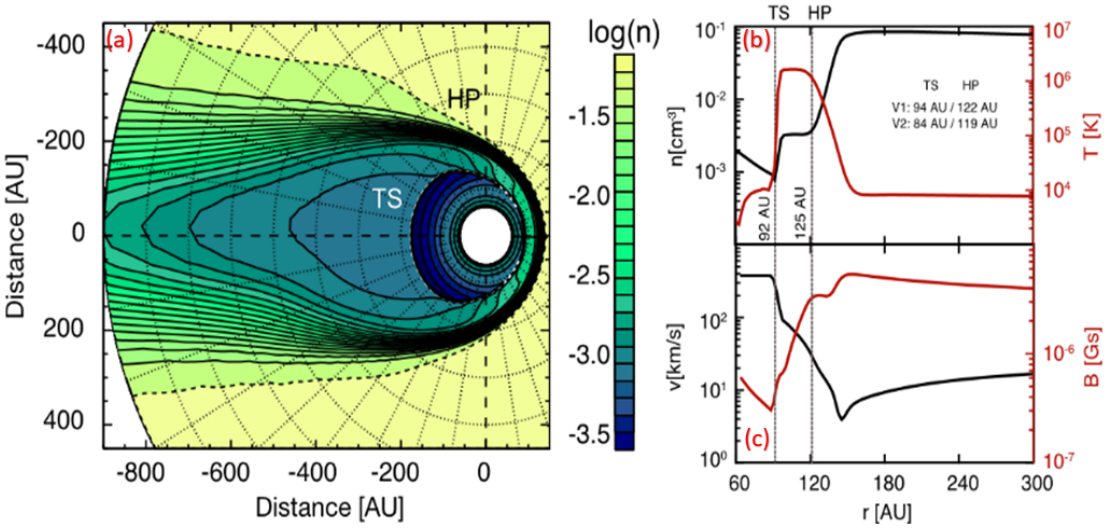

Figure 3.7: *The computed heliospheric environment in terms of density in panel (a), the line of sight for density and temperature in panel (b), HMF magnitude and the plasma speed in panel (c). The interstellar medium is flowing from the right-hand side. The position of the heliospheric pause and the termination shock are shown. Images from: Herbst et al. (2022).*

3.6 Summary and Conclusions

This chapter introduced the reader to the two-dimensional model of Fahr and Kausch (2000), Scherer and Ferreira (2005) and Ferreira and de Jager (2008), the three-dimensional magnetohydrodynamical model developed by Pen et al. (2003) and the Cronos model by Kissmann et al. (2018). The first two models will be used in this work, with the Cronos model results of λ Cephie being compared to simulations in Chapter 5. The cooling function proposed by Mellema and Lundqvist (2002) is included in the two-dimensional model. In the Cronos model, the cooling function of Schure et al. (2009) is used. For now, the Pen et al. (2003) 3D MHD model does not include radiative cooling.

Radiative cooling causes energy loss through radiation emission, primarily affecting the outer astrosheath. As shown in Figure 3.4, a thin, dense shell with a high compression ratio is formed. However, after cooling, the thin outer shell expands again at a later simulation time.

The 3D MHD model of Pen et al. (2003) was used by Strauss (2013) for heliospheric simulations shown in Figure 3.5. The results showed the computed density, solar wind flow speed, HMF magnitude and temperature. The computed HMF magnitude showed similar results as that of Opher et al. (2006). Most recently, Marais (2023) showed that the 3D MHD model by Pen et al. (2003) is influenced by the different

grid sizes, with the profiles becoming smoother when the grid size increases. Note that this model does not yet include radiative cooling.

The Cronos Model is used to simulate the heliospheric structure, as shown in Figure 3.7, and it showed that the TS is located at 92 AU and the HP at 125 AU. These results were in good agreement with that of the Voyager 2 spacecraft data, see Richardson et al. (2022). This model will be used in Chapter 5 to compare the 3D MHD model of Pen et al. (2003) with the results of Baalmann et al. (2020, 2021).

Chapter 4

The effects of different parameters on astrospheric evolution.

4.1 Introduction

In this chapter, the two-dimensional model described in chapter 3 will be used to study the effects of various parameters' on astrospheric evolution. This will be accomplished by comparing the results from each changing parameter with the standard parameters given in Table 4.1. This will be done systematically, with one parameter changed at a time while the others keep their standard values. The parameters include the simulation time, mass loss rate, ISM density, ISM magnetic field, ISM temperature, and stellar wind (SW) outflow speed.

Table 4.1: *Standard parameters assumed in the model.*

Parameters	Standard values
Mass loss rate	2×10^{-6} $M_{\odot}$/year
Outflow speed	1500 km/s
ISM density	1.6726×10^{-23} g.cm^{-3}
ISM temperature	1000 K
ISM magnetic field	3 μG

4.2 Astrospheric evolution structure at different simulation times.

In this section, the astrospheric structure at different simulation times were presented. Figure 4.1 shows the computed density profile for different simulation times when including radiative cooling in the model. The red dotted line shows the model simulation after 50000 years of simulation time, the blue dash-dotted line corresponds to 100000 years, the yellow dashed line corresponds to a simulation time of 150000 years, and the green line corresponds to a simulation time after 200000 years.

As shown in Figure 4.1, the astrosphere expands as time progresses, increasing the size of IAS and OAS. For example, the IAS size increased by ∼3.7 pc when comparing the density profile at 50000 years with the same at a simulation time of 200000 years. Earlier simulation times, such as 50000 years, show a thin, high-density area closer to the IAS that is 0.3 pc in width, due to radiative cooling removing the thermal energy in the region. However, as the simulation time increases, this feature disappears, as can be seen by the two density peaks shown at 100000 years. As time increases, the density distribution changes to the classic non-cooling result.

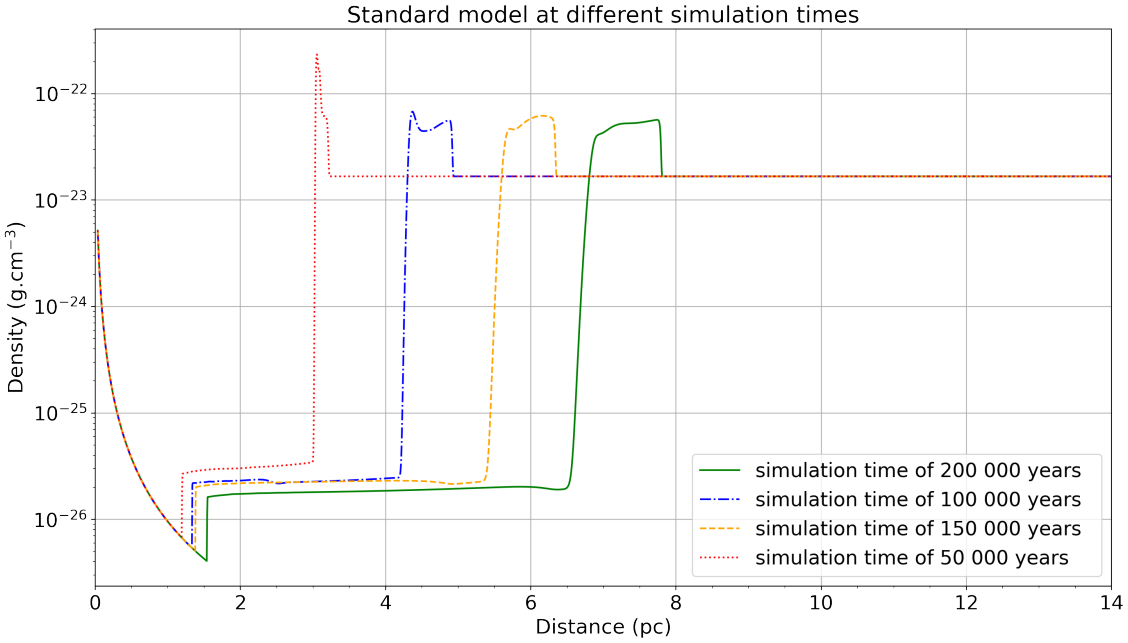

Figure 4.1: *The computed density profile corresponding to different simulation times for standard parameters, including radiative cooling and its effect, is visible at early simulation times, as listed in Table 4.1.*

4.3 Effects of different mass-loss rates on astrospheric evolution.

This section discusses the effects of different mass-loss rates on the structure of the astrosphere as it evolves. The density conversion (as needed in the model) is calculated by assuming the following continuity equation:

$$\rho = \frac{\dot{M}}{4\pi v r^2}. \tag{4.1}$$

The radius, represented by r, is assumed to be the inner boundary of the model at 0.0032 pc. The speed is represented by v, and $\dot{M}$ represents the star mass loss rate. The relationship between the stellar wind ram pressure and the mass loss rate is given by:

$$P_{ram} = \frac{1}{2}\rho v^2. \tag{4.2}$$

This equation shows that the stellar-wind-ram pressure is directly proportional to the stellar-wind density. Figure 4.2 shows the result of Light (2020), wherein the varying density profiles were computed after 200000 years. The changes in the mass loss rate led to different densities at the inner boundary, for example, of 1 particles.cm^{-3} (the blue dotted line), 10 particles.cm^{-3} (solid orange line), 20 particles.cm^{-3} (green dashed line), and 100 particles.cm^{-3} (red dash-dotted line), respectively, using equation 4.1.

Note that a change in the mass loss rate directly affects the ram pressure of the stellar wind, as shown by equation 4.2. An increase in the mass loss rate will increase the ram pressure, thereby causing the distance between the inner boundary, termination shock, astropause, and bow shock to increase, as shown in Figure 4.2. A high mass loss rate results in a later cooling period. Also, cooling occurs earlier for a smaller mass loss rate and has already occurred for the small mass loss rate shown in Figure 4.2.

Table 4.2: *The parameters used in the model illustrate the effect of the mass loss rate on a computed astrosphere, Light (2020).*

Parameters	Values
Simulation time	200000 years
Outflow speed	1000 km/s
ISM density	1 particle.cm^{-3}
ISM temperature	1000 K
ISM magnetic field	3 μG

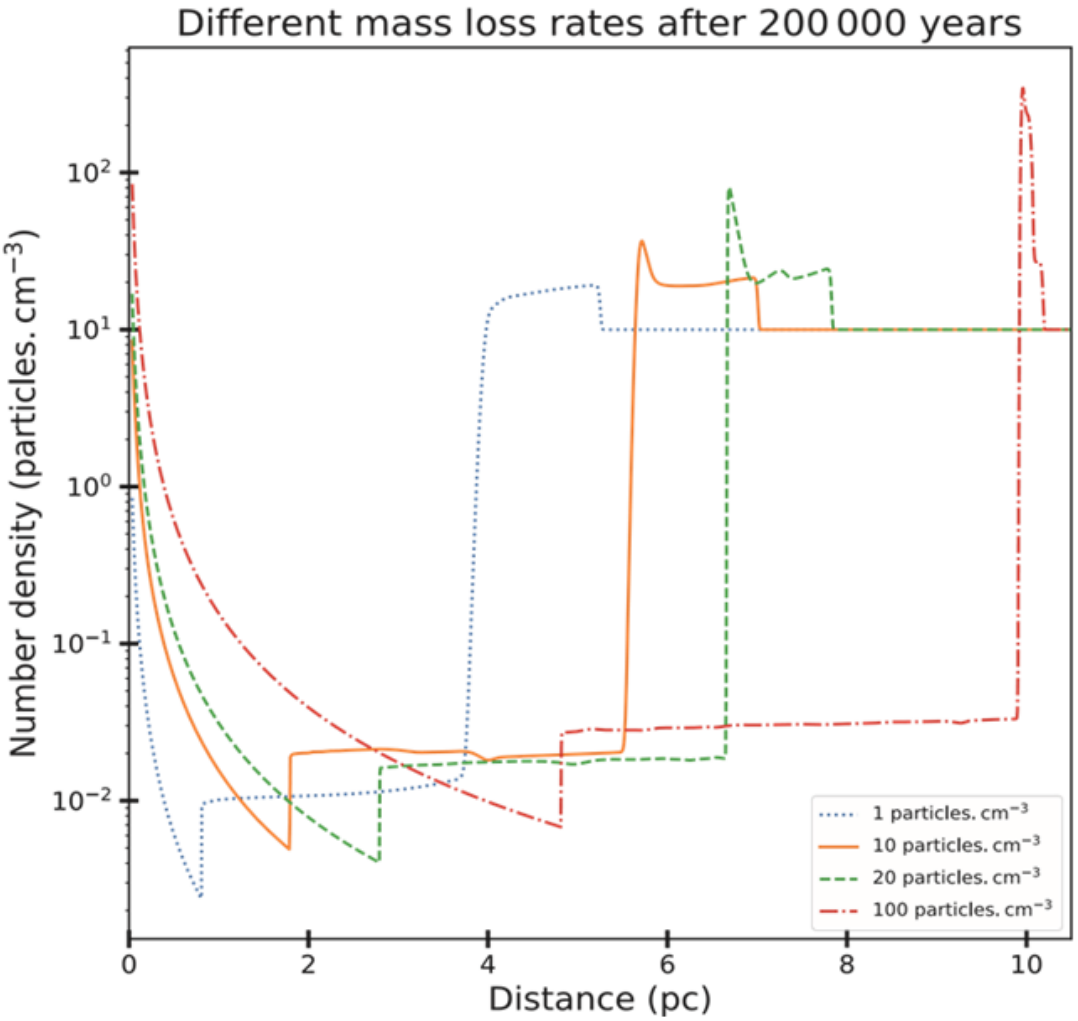

Figure 4.2: *The computed density profile for different mass loss rates. The changes in the mass-loss influence the stellar wind density is as follows: the blue dot line is for ∼1 particle.cm^{-3}, the solid orange line is for ∼10 particles.cm^{-3}, the green dashed line is for ∼20 particles.cm^{-3}, the red dash-dotted line is for ∼100 particles.cm^{-3} at the inner boundary. Image from Light (2020).*

4.4 Effect of the stellar wind outflow speed on the astrospheric evolution

This section discusses the effect of the stellar wind outflow speed on astrospheric evolution utilising the 2D MHD model. Figure 4.3 shows the computed density profile (panel (a)), stellar wind outflow speed profile (panel (b)), temperature profile (panel (c)), compression ratio (panel (d)), bow shock radius (panel (e)), and width of the bow shock (panel (f)) for different stellar wind (SW) outflow speeds when including radiative cooling. The solid black lines represent the standard model parameters, as given in Table 4.1. For this figure, the green dotted lines represent the model simulation corresponding to the outflow speed of 1200 km/s, and the orange dashed lines correspond to the outflow speed of 1800 km/s. All other parameters are given in Table 4.1.

The computed density profile in panel (a) is after 200000 years of simulation time. As already stated, different computed outflow speed scenarios are compared. The panel shows that for slower outflow speeds, the astrosphere size decreases; hence, the position of the termination shock, the astropause, and the bow shock is close to the inner boundary. The stellar wind travels further for the highest outflow speed, leading to a larger astrosphere. Also, note that cooling occurs late because of the high outflow speed scenario. For this scenario, a thin, high-dense area is visible near the astropause; for the remaining options, cooling has already taken place, and the thin shell is relaxed.

The computed outflow speed profile in panel (b) shows a decrease of a factor of ~ 4 in speeds at the termination shock for all the scenarios during the speed transitions from supersonic to subsonic. Afterwards, the outflow speed gradually declines for all scenarios until the interstellar medium flows.

The temperature profile shown in panel (c) is again at 200000 years of simulation time. The figure shows that from 0 to ~ 1.5 pc, the temperature decreases for all outflow speed scenarios until the termination shock. After the termination shock, the temperature increases with the lower SW outflow speed having the lowest temperatures, compared to the high-speed scenarios due to the large kinetic energy, which converts to thermal energy. Furthermore, a cool astrosheath is visible close to the bow shock for the high outflow speed scenario due to the late cooling compared to the other scenarios.

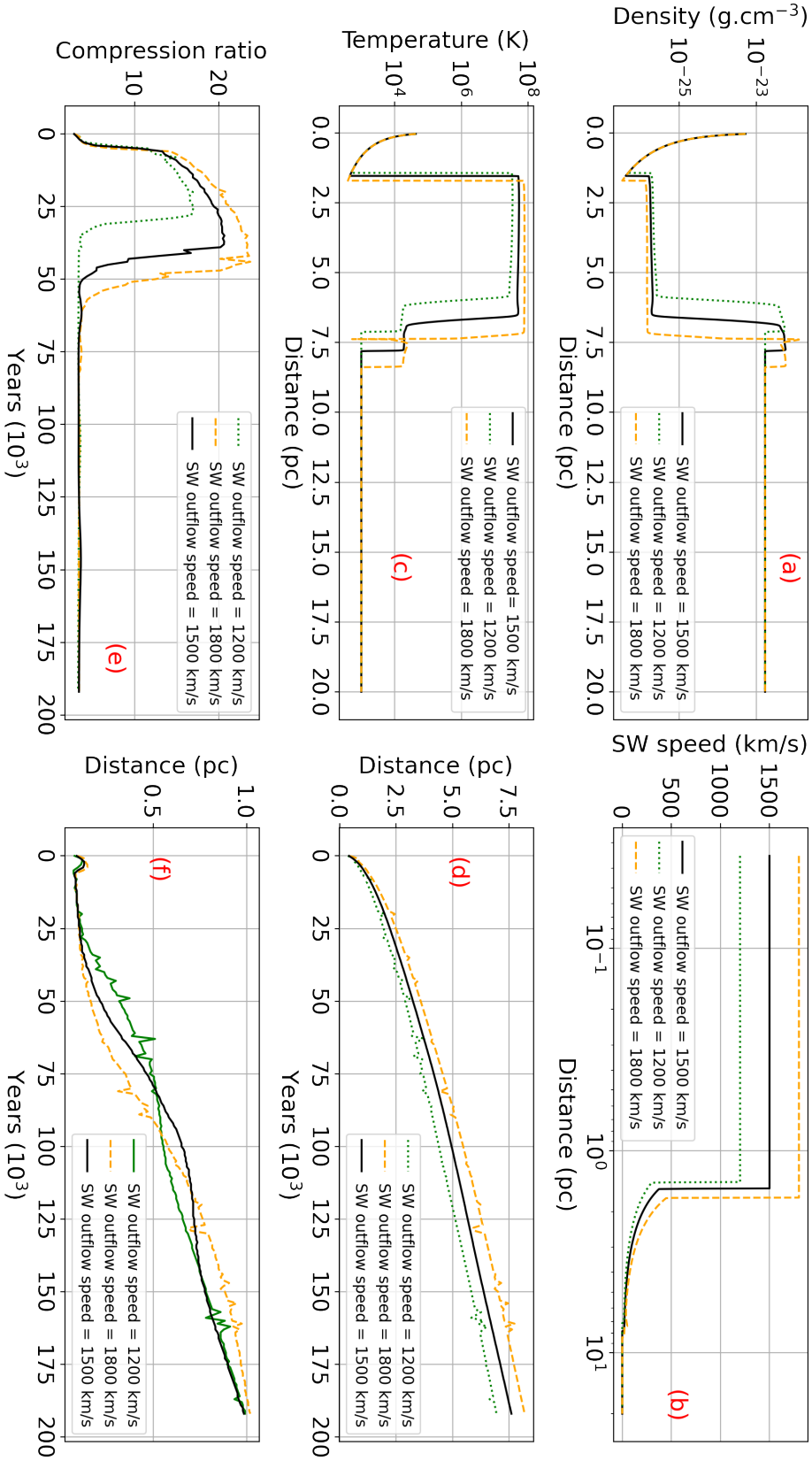

Figure 4.3: *Simulations corresponding to different computed stellar wind outflow speeds. The figure shows the density profile (panel (a)), SW outflow speed profile (panel (b)), temperature profile (panel (c)), bow shock radius (panel (d)), compression ratio (panel (e)), and bow shock width (panel (f)). Three different SW outflow speeds are shown: 1800 km/s (dashed orange line), 1500 km/s (solid black line) and 1200 km/s (green dotted line).*

Panel (e) shows the compression ratio as a function of the simulation time. Visible here are the effects of cooling, where the compression is much larger compared to pure hydrodynamic shocks, where the compression ratio is expected to be ∼4. After ∼75000 years or so, radiative cooling no longer influences the simulations and the value of ∼4 is reached. However, between 0 and ∼ 53000 years, the compression ratio for all scenarios is much higher than 4, with the higher SW outflow speed having a maximum compression ratio of ∼24. For a lower outflow speed, the bow shock becomes less compressed than the other scenarios in its earliest years. Note that in higher SW outflow speed scenarios, e.g. 1500 km/s and 1800 km/s, the compression ratio is much larger, with the highest difference between 1200 km/s and 1800 km/s being ∼7.

The bow shock distance (radius) as a function of simulation time for all the scenarios is shown in panel (d). The BS radius increases for all the scenarios as a function of time, with the highest outflow speed resulting in the largest BS radius. The expansion of the bow shock is directly proportional to the outflow speed. Panel (f) shows the width of the bow shock as a function of the simulation time for the different scenarios again. The BS width increase is initially faster up to ∼75000 years, for a lower outflow speed, whereafter it stays constant and then increases later. For high outflow speeds, the opposite occurs. The width first increases slowly compared to other scenarios up to ∼75000 years, and thereafter, it increases fast.

4.5 Effects of different ISM densities on astrospheric evolution

This section shows the effect of different ISM densities on astrospheric evolution. With radiative cooling included, the model results corresponding to three ISM densities are shown in Figure 4.4. The density profile (panel (a)), compression ratio as a function of simulation time (panel (b)), bow shock radius as a function of simulation time (panel (c)) and bow shock width (panel (d)) are shown. Apart from the different ISM densities, the parameters used in the model are given in Table 4.1. The computed ISM density scenarios are as follows: The solid black line shows the standard ISM density, the red lines show the ISM density of 8.3631×10^{-23} g.cm^{-3}, and the blue lines show the ISM density of 1.6726×10^{-22} g.cm^{-3}.

The density profiles in panel (a) show that the astrosphere size is smaller for a high ISM density. The IAS regions shrink in size, with the largest difference in the IAS

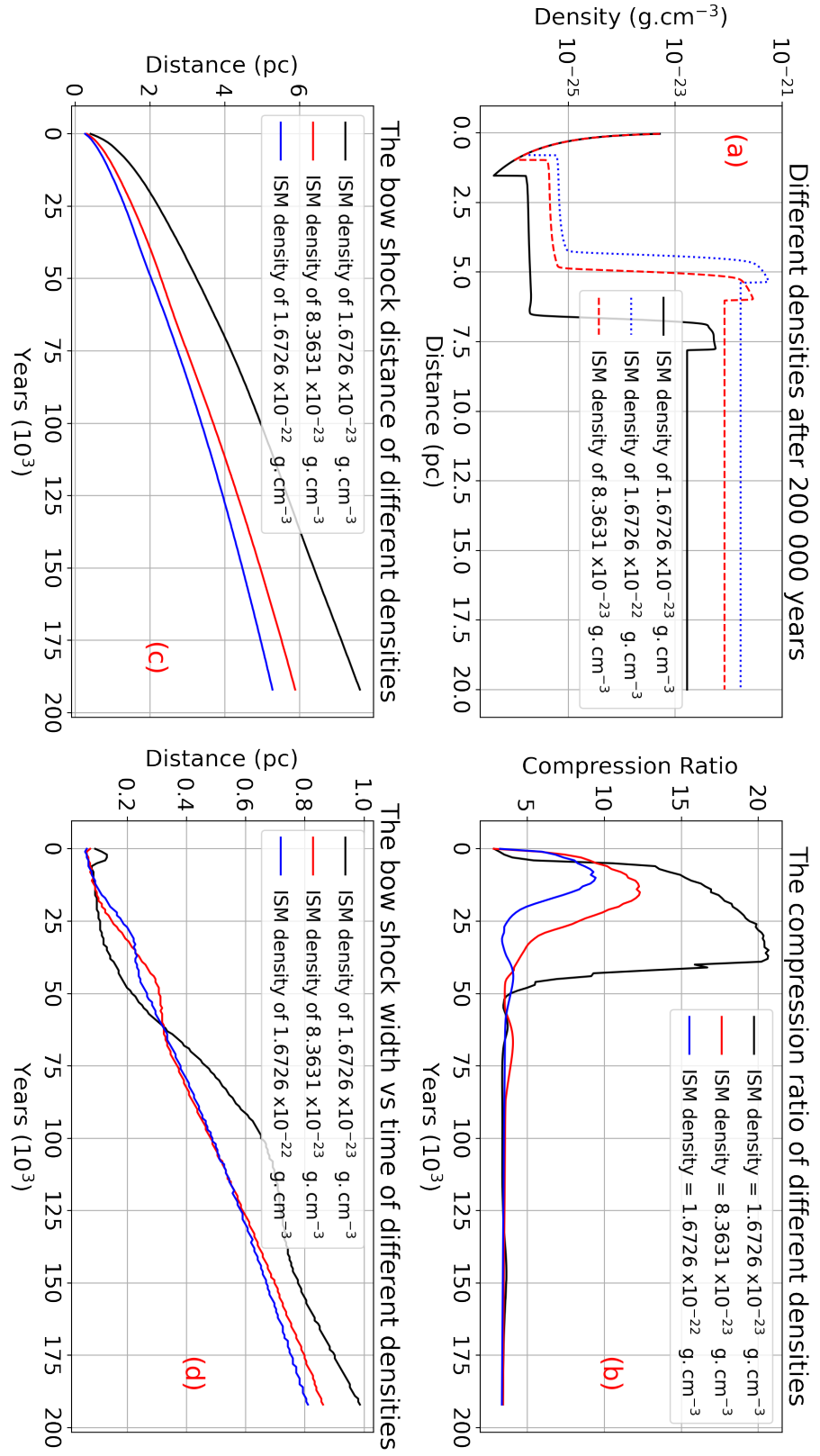

Figure 4.4: *The astrosphere structure for three different ISM densities when all the other parameters are the standard values shown in Table 4.1. The density profile is shown in panel (a), the compression ratio is shown in panel (b), the bow shock radius as a function of simulation time is shown in panel (c), and the bow shock width as a function of simulation time is shown in panel (d).*

occurring between the ISM density of 1.6726 $\times 10^{-23}$ g.cm^{-3} and 1.6726 $\times 10^{-22}$ g.cm^{-3}, showing a decrease in size by $\sim$2.3 pc. For a higher ISM pressure, the size of the astrosphere reduced, increasing the post-shock density of the stellar wind.

The compression ratio as a function of the simulation time is shown in panel (b). The higher the ISM density, the lower the compression ratio in the first $\sim$50000 years due to cooling. For example, the maximum compression ratio between the ISM density of 1.6726 $\times 10^{-23}$ g.cm^{-3} and 1.6726 $\times 10^{-22}$ g.cm^{-3} has a difference of $\sim$45.64%. Furthermore, the larger the ISM density, the sooner cooling occurs, and the compression is reduced to the standard hydrodynamic value.

Panel (c) shows the bow shock's radius as a function of simulation time. As expected, the radius is much smaller for a higher ISM density. In panel (d), the width of the bow shock as a function of simulation time shows an increase in width as simulation time progresses. However, the rate of this increase varies across the scenarios corresponding to different interstellar medium densities. There is a slower rate of increase during the early stages for scenarios with a lower ISM density, which is higher at later stages, in contrast to those with a higher ISM density.

4.6 Effect of the interstellar magnetic field on the astrospheric evolution

This section studies the ISM magnetic field's effects on the astrosphere's evolution. Magnetic fields play an integral part in the interstellar medium, and their magnitude may vary based on the environmental circumstances (Beck, 2009). As a result, during the expansion of the stellar wind into the interstellar medium, the stellar wind ram pressure interacts with the interstellar pressures, notably the thermal pressure (if the ISM is hot), constraining the expansion. If an interstellar magnetic field is present, it introduces a third pressure known as the ISM magnetic pressure, which, depending on its strength, can potentially impact the morphology of the astrosphere. Additionally, if the magnetic field lines embedded in the ISM are initially pushed outward by the wind, then in the shocked outer shell, these magnetic field lines are forced together, increasing magnetic pressure. However, the increased magnetic pressure is insufficient to prevent the star wind from expanding (van Marle et al., 2015), but may affect the compression and cooling.

Figure 4.5 shows the effects of the ISM magnetic field on the model solutions when

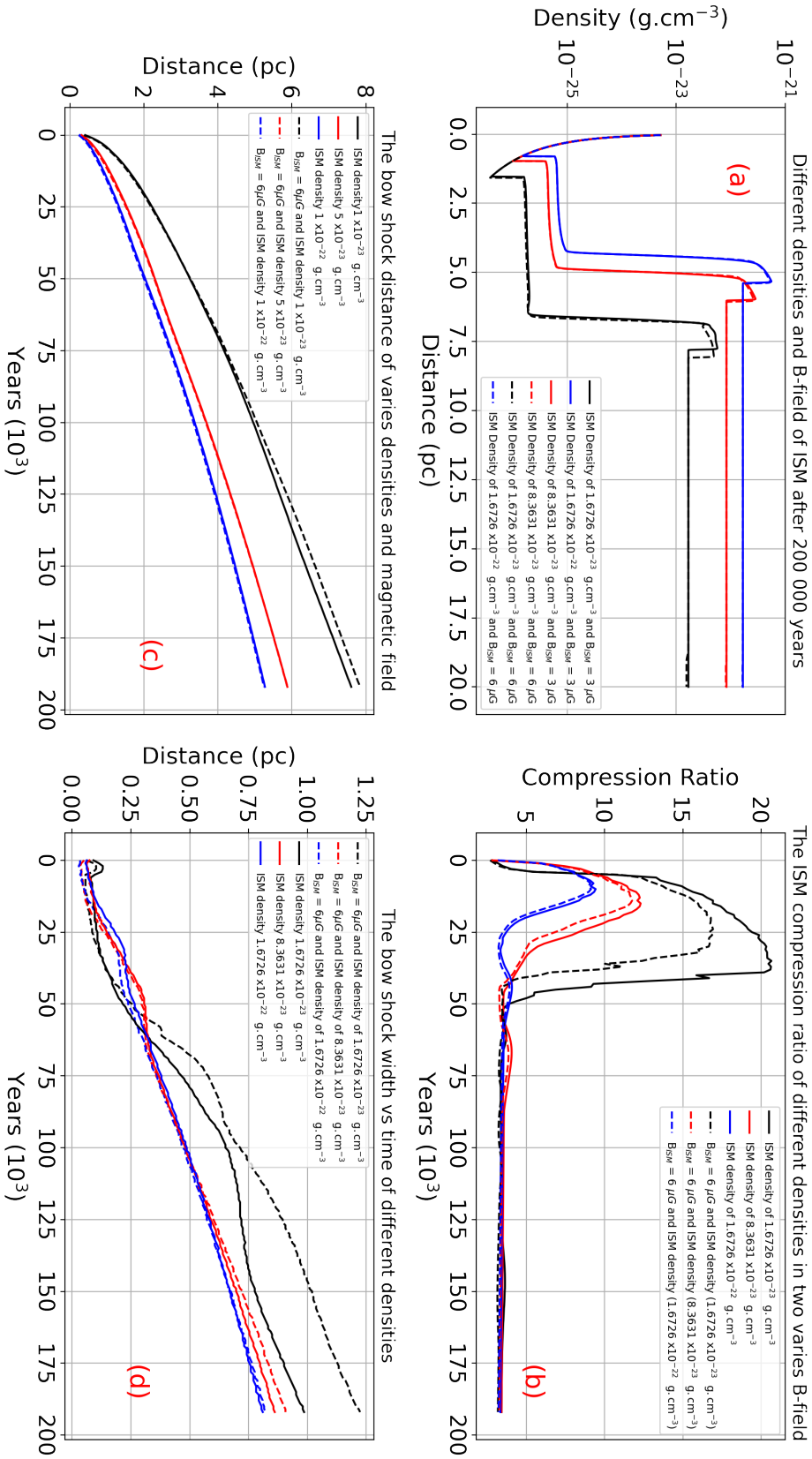

Figure 4.5: *The astrosphere structure for different ISM densities and two different ISM magnetic fields. The solid lines correspond to the different ISM densities with an ISM magnetic field of 3μG. The dashed line corresponds to the different ISM densities with an ISM magnetic field of 6μG. Panel (a) corresponds to the density profile, panel (b) is the compression ratio as a function of simulation time, panel (c) is the bow shock radius as a function of simulation time, and panel (d) is the bow shock width.*

Table 4.3: *Parameters changed in the model.*

Parameters	Values
Simulation time	200000 years
ISM density	1.6726 $\times 10^{-23}$ g.cm^{-3}
ISM density	8.3631 $\times 10^{-23}$ g.cm^{-3}
ISM density	1.6726 $\times 10^{-22}$ g.cm^{-3}
ISM temperature	1000 K
ISM magnetic field	3 μG
ISM magnetic field	6 μG

the field strength is changed from 3 μG (as in the previous figure) to 6 μG. The density profile (panel (a)), compression ratio as a function of simulation time (panel (b)), bow shock radius as a function of time (panel (c)) and the bow shock width as a function of simulation time (panel (d)) are again shown. The inner boundary remains at 0.0032 pc, and the parameters changed in the model are given in Table 4.3. The solid lines represent different ISM densities, having an ISM magnetic field of 3 μG. The dashed lines show the same ISM densities, but with the ISM magnetic field increased to 6 μG.

Panel (a) shows the computed density profiles after 200000 years of simulation time. The astrosheath size remains unchanged for the high ISM density, irrespective of the magnetic field value. For the lowest ISM density scenario, the size of the outer astrosheath increases when the magnetic field increases. There is a slight increase in the bow shock width with a difference of $\sim$0.01 pc computed.

Panel (b) shows the compression ratio as a function of the simulation time. When a high interstellar medium magnetic field is present, the maximum compression ratio decreases for all scenarios shown. For instance, in this scenario, for an ISM density of 1.6726 $\times 10^{-23}$ g.cm^{-3}, the ratio in compression between a low ISM magnetic field and a high ISM magnetic field is 0.81 in this scenario. As the ISM density increases, the difference between the two magnetic-field scenarios becomes less.

Panel (c) shows the bow shock radius as a function of the simulation time for the three different ISM densities and different ISM magnetic fields. As expected, the magnetic field magnitude is only important for the lowest ISM density scenario. At high ISM densities, this effect is not visible.

Panel (d) shows the bow shock's width as a function of simulation time. As the interstellar medium magnetic field strength increases, the width of the bow shock also increases due to the added pressure. This effect is particularly pronounced in scenarios with a low ISM density. It is worth noting that this effect is not as evident

in high ISM density scenarios. Note that due to the limitation of the 2D model, the ISM magnetic field was assumed to be azimuthal everywhere azimuthal causing the field to be perpendicular to the direction of the outflow.

4.7 The effects of different ISM temperatures on astrospheric evolution

This section discusses the effect of different ISM temperatures on astrospheric evolution. The ISM temperature in the model increased from 1000 K to 10000 K in the model. The density profile (panel (a)), compression ratio as a function of simulation time (panel (b)), bow shock radius as a function of time (panel (c)) and the bow shock width as a function of simulation time (panel (d)) are shown. The inner boundary remains at 0.0032 pc, and other parameter changes in the model are shown in Table 4.4. All solid lines shown in Figure 4.6 have an ISM temperature of 10^3 K, and the dashed lines have an ISM temperature of 10^4K.

Table 4.4: *The model parameters.*

Parameters	Values
ISM density	1.6726×10^{-23} g.cm^{-3}
ISM density	8.3631×10^{-23} g.cm^{-3}
ISM density	1.6726×10^{-22} g.cm^{-3}
ISM magnetic field	3 μG

The density profile (in panel (a)) after 200000 years of simulation time shows that the size of the inner astrosheath decreases in scenarios characterised by a high interstellar medium temperature. On the other hand, the width of the bow shock increases for high-temperature scenarios. Also, the maximum density found in the bow shock decreases when temperatures are assumed to be larger.

The compression ratio as a function of simulation time (in panel (b)) shows that at high ISM temperatures, the computed compression ratio becomes ∼4, earlier compared to a lower temperature. The maximum compression ratio decreases for all high-ISM temperature scenarios.

The radius of the bow shock as a function of simulation time (in panel (c)) shows that for a larger ISM temperature, the radius of the bow shock is slightly larger at the end of the simulation time. The largest difference occurred between the two ISM temperature scenarios at high ISM densities due to the temperature dependence of

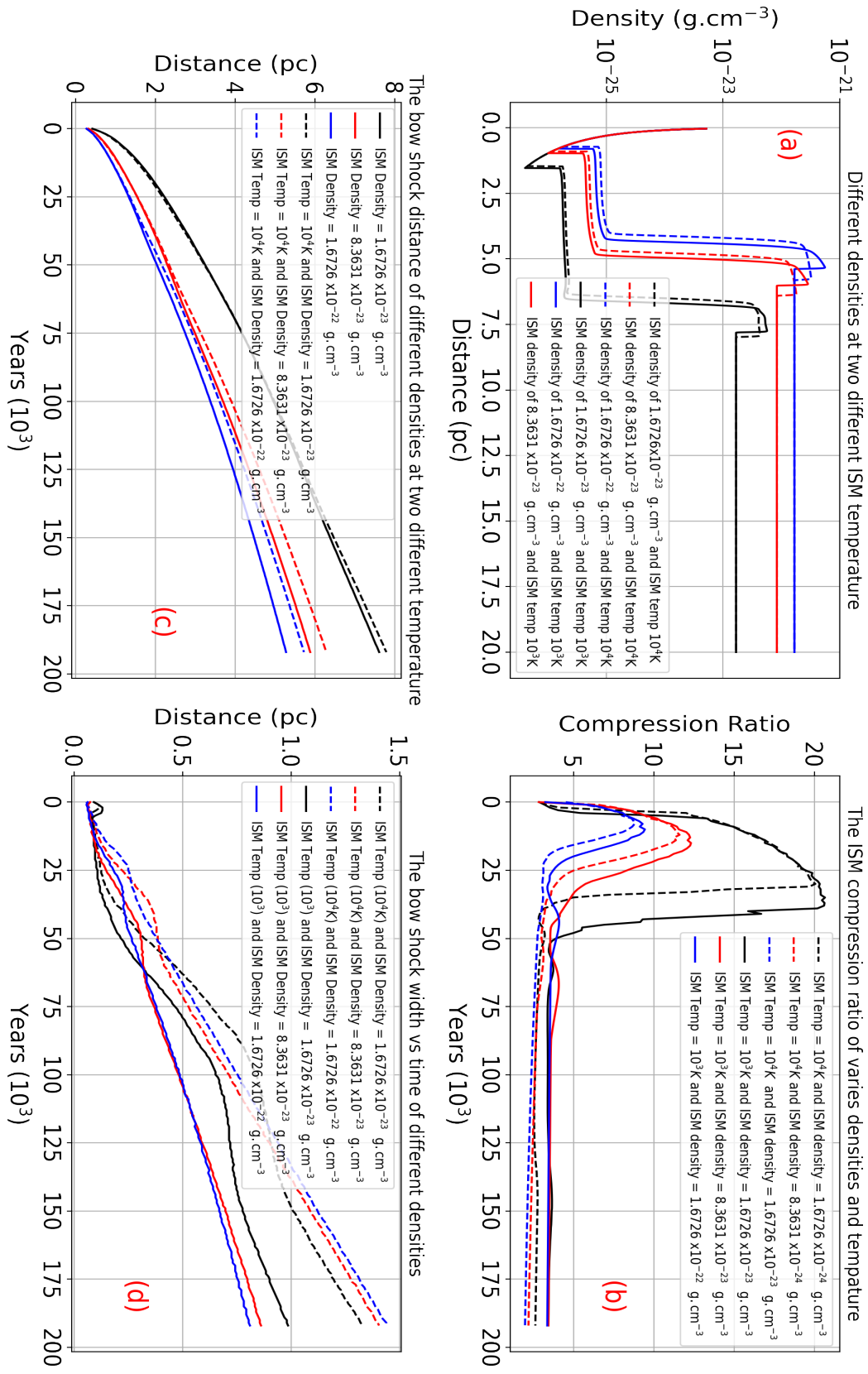

Figure 4.6: *A computed astrospheric structure corresponding to different ISM densities and two different ISM temperatures. The density profile is shown in panel (a), panel (b) the compression ratio as a function of simulation time, panel (c) the bow shock radius as a function of simulation time, and panel (d) the bow shock width as a function of simulation time. The solid lines show scenarios corresponding to an ISM temperature of 1000 K, whereas the dashed lines show the differences in ISM density with an ISM temperature of 10000 K.*

the cooling function, as shown in Figure 4.6.

The bow shock width as a function of simulation time, in panel (d) shows an increase in this value as the ISM temperature increases for all the different ISM densities, with the highest ISM density being the most influenced.

4.8 Summary and Conclusions

The chapter has shown how various parameters affect the evolution of the astrosphere. As shown in Figure 4.1, the simulation time is important as the astrosphere evolves into the interstellar medium. The effect of the mass loss rate is also shown in Figure 4.2, showing that the larger the mass loss rate, the larger the density will be at the inner boundary, thus increasing the size of the astrosphere. The effects of stellar wind outflow speed are shown in Figure 4.3, where it is evident that an increase in outflow speed increases the astrospheric cavity and increases thermal energy after the TS up to the BS.

The effect of the ISM density is shown in Figure 4.4, showing that a high ISM density can reduce the astrosphere's size while a lower density has the opposite effect. The ISM magnetic field strength was also shown in Figure 4.5, showing that this parameter mostly impacts the astrosphere's outer structure. This effect is, however, mitigated in scenarios with a significant ISM density. In Figure 4.6 the impact of the ISM temperature affected the positioning of the maximum BS, with the high density increasing faster as the simulation time increased.

Chapter 5

Astrosphere of λ Cephei

5.1 Introduction

This chapter presents the model results of the astrospheric structure of λ Cephei. The three-dimensional model of Pen et al. (2003) is compared to that of Baalmann et al. (2021), who used the model of Kissmann et al. (2018). The effect of the relative velocity of the evolution of this astrosphere is briefly shown, as well as the effect of the ISM magnetic field strength and orientation on λ Cephei's astrosphere using the Pen et al. (2003) model.

5.2 λ Cephei

λ Cephei is a blue runaway supergiant of spectral type O6.5 with an apparent magnitude[1] of + 5.05 in V band and a luminosity[2] of 6.3 $\times 10^5$ $L_\odot$ (Bouret et al., 2012). λ Cephei has a mass loss rate of $\dot{M} = 6.8 \times 10^{-6}$ $M_\odot$/yr with a relative velocity of 80 km/s relative to its local interstellar medium and a high stellar wind speed of 2500 km/s, resulting in the formation of the bow shock and astrosphere extending several parsecs, as per Scherer et al. (2016b) and Baalmann et al. (2021, 2020). Bouret et al. (2012) calculated the distance from Earth to λ Cephei (d_0) as 950 pc. However, Gaia Collaboration (2018) showed that $d_0 = 617$ pc when using the Gaia (Global Astrometric Interferometer for Astrophysics) measurement.

[1] Apparent magnitude is the brightness of an object as it appears to an observer on Earth (Ferreras, 2019).

[2] Luminosity is a measure of the total amount of power or energy emitted by a star or other celestial object per time (Ferreras, 2019).

5.3 Observations

This section shows recent images captured near λ Cephei, as shown by Baalmann et al. (2020) in Figure 5.1. These images were reproduced by combining observational data from three distinct infrared bands observed through the Wide-field Infrared Survey Explorer (WISE, Wright et al., 2010, in panel (a)), the Multiband Imaging Photometer for Spitzer (MIPS, Werner et al., 2004, and Rieke et al., 2004, in panel (b)), and the Hα emissions obtained from the INT Photometric Hα Survey of the Northern Galactic Plane (IPHAS, Drew et al., 2005, and Barentsen et al.,2014, in panel (c)).

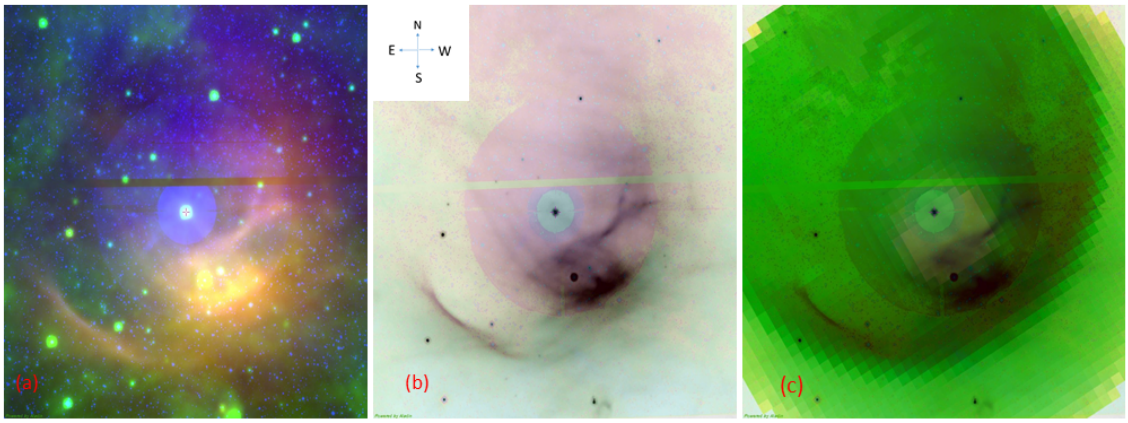

Figure 5.1: *Images of λ Cephei around its local interstellar medium. Panel (a) shows the observation using WISE in three infrared bands, panel (b) corresponds to the grey scale MIPS observation of λ Cephei, and panel (c) shows the Hα simulated composite observation from IPHAS. λ Cephei is placed at the centre of all the panels and is marked by the magenta cross. Images from Baalmann et al. (2020).*

Figure 5.1 shows that the star is moving in the south-southwest direction (in the figure, east to the left and west to the right), resulting in the faint visibility of a bow shock in Hα as well as in the infrared, and is visible as a broad arc southeast to the west of the star in the longwave infrared spectrum. The astropause is shown by the infrared emission structure near the BS. In Hα, the internal structure of the astrosphere is not visible. Scherer et al. (2020) proposed that the lack of visibility of the inner astrosphere, particularly the region from the λ Cephei to the astropause, may be attributed to the low number density ranging from 10^{-3} to 10^{-2} cm^{-3}. Additionally, despite a highly heated inner astrosheath, the emission of X-rays or Hα is notably subdued due to the energy being far below the range of the observational instruments. For a more detailed analysis that includes the observation of total fluxes of synchrotron radiation and bremsstrahlung, also, Hα flux, see Baalmann et al. (2020) and Scherer et al. (2020). For details such as the thermal plasma, ram

pressure, and the total pressure beta, see Baalmann et al. (2021).

5.4 Cronos model

This section discusses the simulations of Scherer et al. (2016b, 2020) and Baalmann et al. (2021), who used the Cronos model of Kissmann et al. (2018). Table 5.1 shows the parameters for the model, where a spherical grid was performed, with a resolution of $N_r \times N_\vartheta \times N_\varphi = 990 \times 30 \times 60$ cells. Figure 5.2 shows the results as a polar contour plot.

Table 5.1: *The parameters used in the model to compute the astrosphere of λ Cephei using the Cronos model. From Scherer et al. (2020) and Baalmann et al. (2021).*

Region	Parameter	value
ISM	Density	1.8399×10^{-23} g.cm^{-3}
ISM	Temperature	10000 K
ISM	Speed	80 km/s
ISM	Magnetic field strength	10 μG
–	Inner boundary	6000 AU
SW	Density	6.8578×10^{-24} g.cm^{-3}
SW	Temperature	1000 K
SW	Speed	2500 km/s
SW	Magnetic field strength	0.67 μG
–	Cooling function	Schure et al. (2009)

Figure 5.2 shows the expected bullet-shape polar contour plot of the outflow speed (in black) with density (shown by the colour bar). The ISM inflow is from the right to the left. From the star to the nose, the astrosphere is $\sim$ 2.3 pc, but it extends more than 10 pc from λ Cephei to the astrotail. The computed density shows that, in all the directions from the λ Cephei, the density decreases up to the termination shock and subsequently increases. The astropause and bow shock were shown to have high densities. Note that the black polar contour plot only shows the changes in the outflow speed.

Figure 5.3 shows a radial plot obtained by selecting a cut in Figure 5.2 at an angle of 0^o (extending from the star towards the nose). The black line shows the computed density, while the blue line shows the computed speed. The positions of the termination shock (TS), the astropause (AP), and the bow shock (BS) are shown in Figure 5.3. Similar to Figure 5.2, a decrease in the density is shown until the termination shock (TS), followed by an increase from $\sim 2.2 \times 10^{-26}$ g.cm^{-3} to $\sim 8.5 \times 10^{-26}$

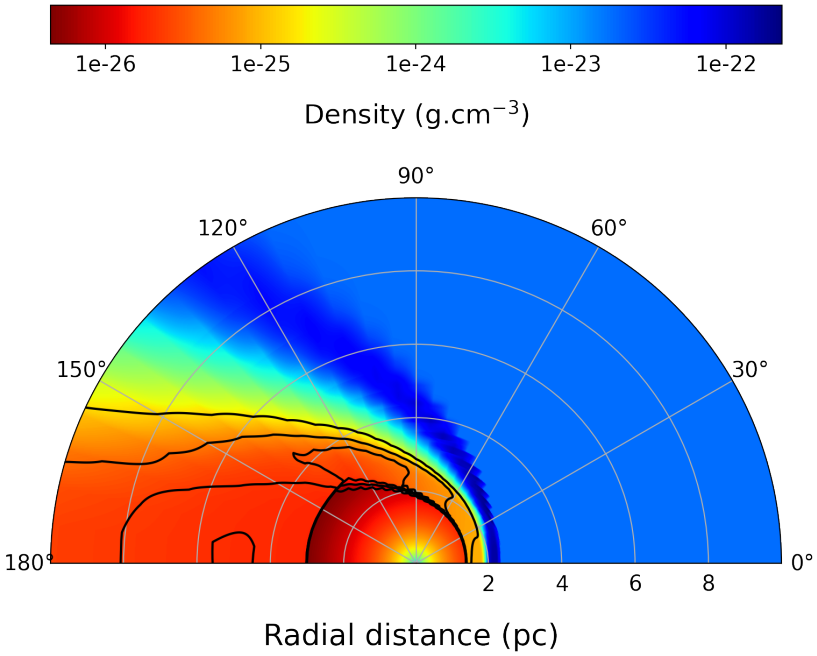

Figure 5.2: *The computed astrosphere of λ Cephei as a polar contour plot in the meridional plane using the Cronos model of Kissmann et al. (2018). The colour bar shows changes in density, and the black contour shows changes in outflow speed. Data from Scherer et al. (2020).*

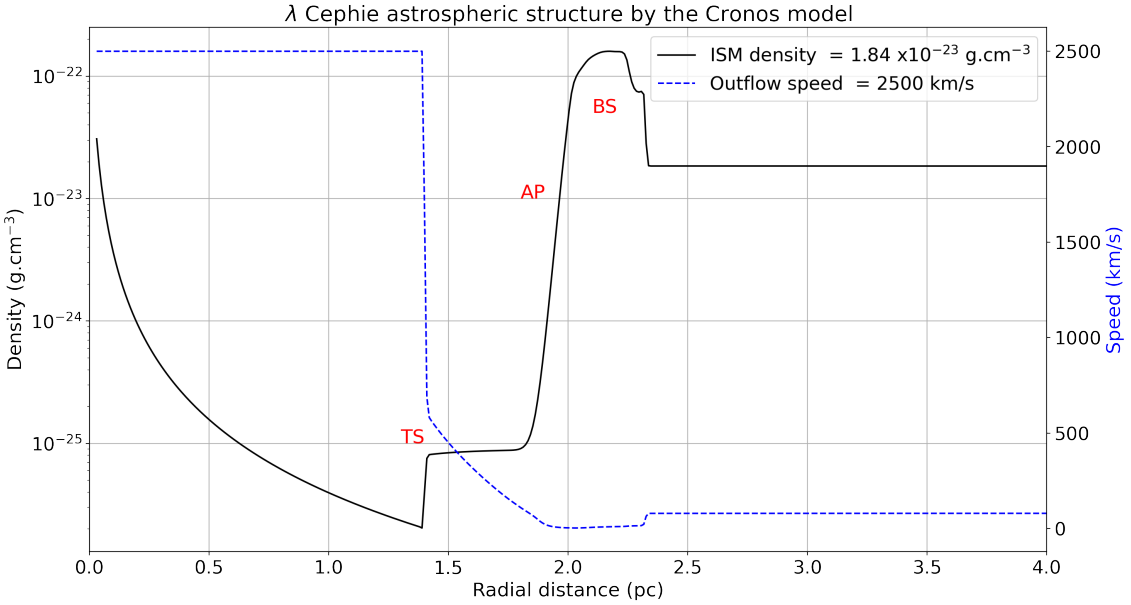

Figure 5.3: *The computed radial plot in the meridional plane from the Cronos model in the direction of λ Cephei to the nose of the astrosphere (the cut is made at an angle of 0°).*

g.cm^{-3}. The outflow speed transitions from supersonic to subsonic, decreasing by a factor of ∼4. At the astropause (AP), there is an increase in density, coupled with a gradual decrease in the outflow speed from ∼620 km/s to 0 km/s. The density peaks in the bow shock region.

5.5 Comparing the two 3D MHD models

This section compares the 3D MHD model of Pen et al. (2003) with the results of the Cronos model from Scherer et al. (2016b, 2020) and Baalmann et al. (2021) discussed in section 5.4. Table 5.2 shows the parameters for the Pen et al. (2003) model.

Table 5.2: *The parameters used in the model to compute the astrosphere of λ Cephei using the 3D MHD model by Pen et al. (2003).*

Region	Parameter	value
ISM	Density	1.84 $\times 10^{-23}$ g.cm^{-3}
ISM	Temperature	10000 K
ISM	Speed	80 km/s
SW	Density	6.977 $\times 10^{-24}$ g.cm^{-3}
SW	Temperature	1000 K
SW	Speed	2500 km/s

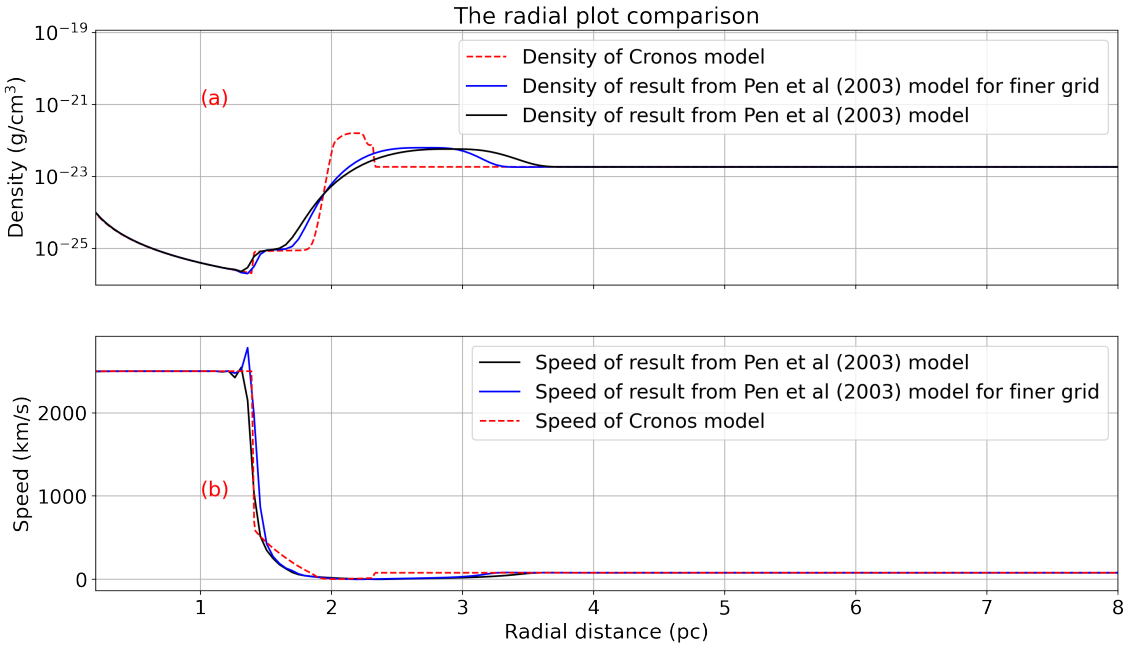

Figure 5.4: *The computed radial plot showing the comparison between the Cronos and Pen et al. (2003) model in the nose direction. Panel (a) shows the compared densities and panel (b) shows the compared outflow speeds.*

The model results from Pen et al. (2003) model and Baalmann et al. (2021) are compared in Figure 5.4. The inner boundary of the two models was different, and the comparison in the figure, therefore, covers a radial distance ranging from 0.2 to 8 pc. The red line represents the Cronos model, while the solid black and blue line represents the simulation from the Pen et al. (2003) model. But the blue line represents a finer grid.

All the scenarios indicated show similar results, from the λ Cephei to the termination shock, but differences occur beyond this point. The Pen et al. (2003) model shows a much smoother radial profile up to the boundary, while the Cronos model shows more detailed features. Although linearly shown on the y-axis, the speeds seem to agree better.

In the bow shock, the Cronos model shows a higher peak density compared to the wider BS width of the Pen et al. (2003) model (black line). This effect may be attributed to radiative cooling, as the Pen et al. (2003) model does not yet include this, but the Cronos model does. For a finer grid (blue line), the BS width decreased for the Pen et al. (2003) model. The difference could, therefore, also be due to the much coarser grid assumed in the Pen et al. (2003) model. If radioactive cooling and a coarser grid are appropriately accounted for in the Pen et al. (2003) model, it is anticipated to yield results similar to those obtained with the Cronos model. Consequently, the Cronos model is deemed to provide the most accurate results for the transition from the OAS to the ISM region for λ Cephei.

5.6 λ Cephei relative velocity

Runaway stars can experience changes in their radial velocity due to gravitational interactions, encounters with other celestial objects, and other astrophysical processes (Bromley et al., 2009) and Ferreras (2019). As a result, this section shows the effect of the relative velocity on the astrosphere of λ Cephei. The relative velocity is reduced from 80 km/s to 40 km/s in the Pen et al. (2003) model, and the results are compared with each other.

Figure 5.5 shows the effect of the relative velocity (V_{rel}) on the size of the astrosphere for λ Cephei. The figure shows the density and outflow speed with the arrows corresponding to the outflow and inflow speeds. The relative velocity changes from 80 km/s (in Figure 5.5(a)) to 40 km/s (in Figure 5.5(b)). All other parameters are

the same as in Table 5.2.

Figure 5.5(b) shows that in all directions when $V_{rel} = 40$ km/s the astrosphere size expands. The expansion increases the position of the termination shock, astropause and bow shock, and the bow shock thickness expands.

A more quantitative comparison of the two figures is shown in Figure 5.6, which shows the radial profiles. For Figure 5.6, the blue lines (solid or dash-dotted) correspond to $V_{rel} = 40$ km/s and the green lines (solid or dash-dotted) correspond to $V_{rel} = 80$ km/s. The dash-dotted lines show the speed, and the solid lines show the density.

The figure shows that when relative velocity decreased to 40 km/s, the size of the astrosphere increased. The inner astrosheath increased by ∼0.6 pc and the outer astrosheath by ∼0.75 pc, from the star to the nose.

5.7 Interstellar magnetic field

In this section, the Pen et al. (2003) model is again used to study the effect of a significantly increased ISM magnetic field on a computed astrospheric structure of λ Cephei. The model uses Parker's field expression to define the inner boundary and two different ISM magnetic field values for the two scenarios shown. Figure 5.7 shows contour plots in the azimuthal plane corresponding to two distinct strengths of the ISM magnetic field. All parameters, except the ISM magnetic field (B_{ISM}), are the same as in Table 5.2. Figures 5.7(a) corresponds to $B_{ISM} = 10^{-7}$ G, while Figure 5.7(b) corresponds to the $B_{ISM} = 10^{-5}$ G. The arrows within the figures indicate the direction of the magnetic field.

As stated previously, Figure 5.7(a) shows the contour plot corresponding to a computed ISM magnetic field at 10^{-7} G, with the direction of the ISM magnetic field indicated by arrows. As with the HMF, the rotational movement of the λ Cephei creates the AMF lines to adopt the shape of an Archimedean spiral near the star, indicated by the arrows as well as the circle near the star. Similar to the HMF, the computed magnetic field strength decreases radially in all directions until the TS, where it increases. Afterwards, the computed magnetic field strength increases again at the AP, with the strongest field shown in the BS region.

Figure 5.7(b) shows the ISM magnetic field strength when 10^{-5} G is assumed in

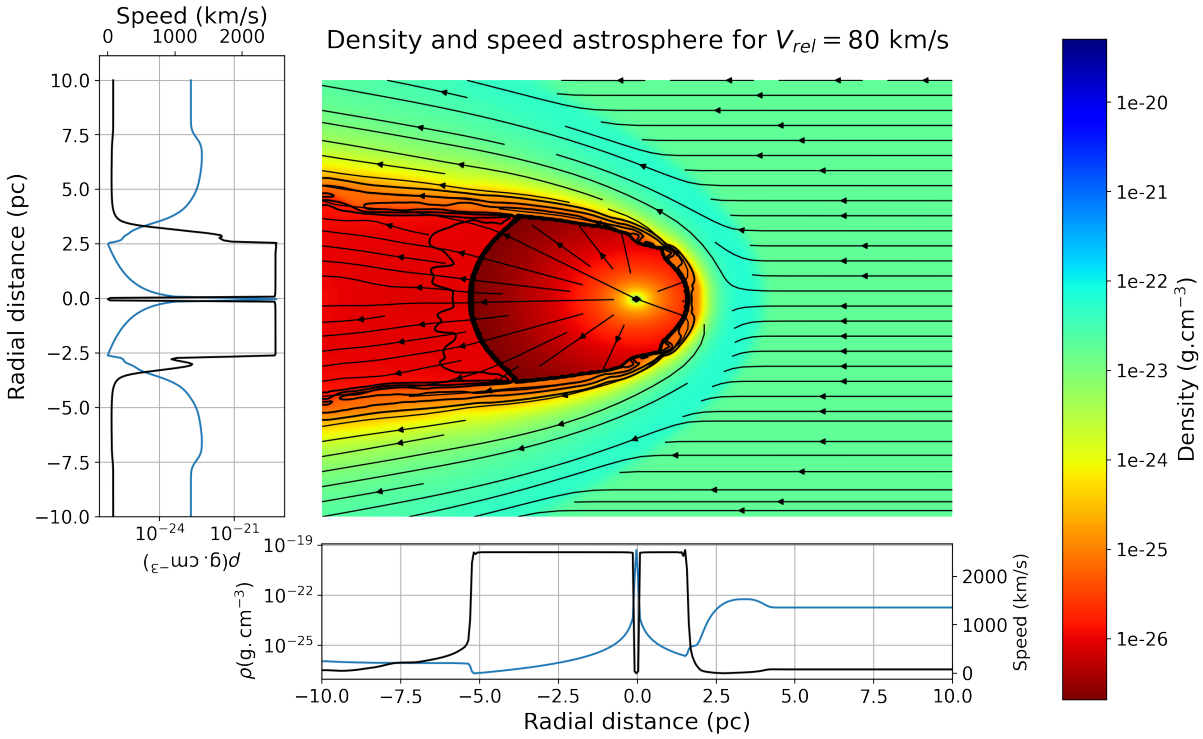

(a) Contour plot for $V_{rel} = 80$ km/s.

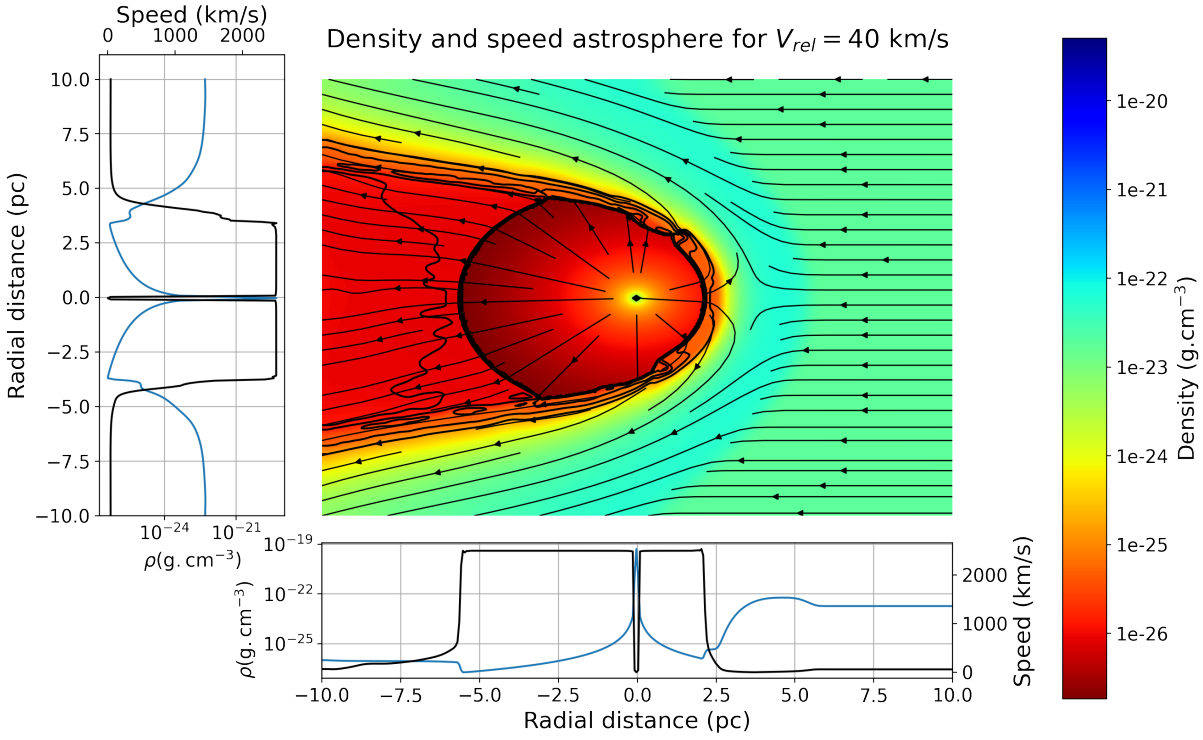

(b) Contour plot for $V_{rel} = 40$ km/s.

Figure 5.5: *Computed λ Cephei astrosphere as contour plots for the different relative velocities.*

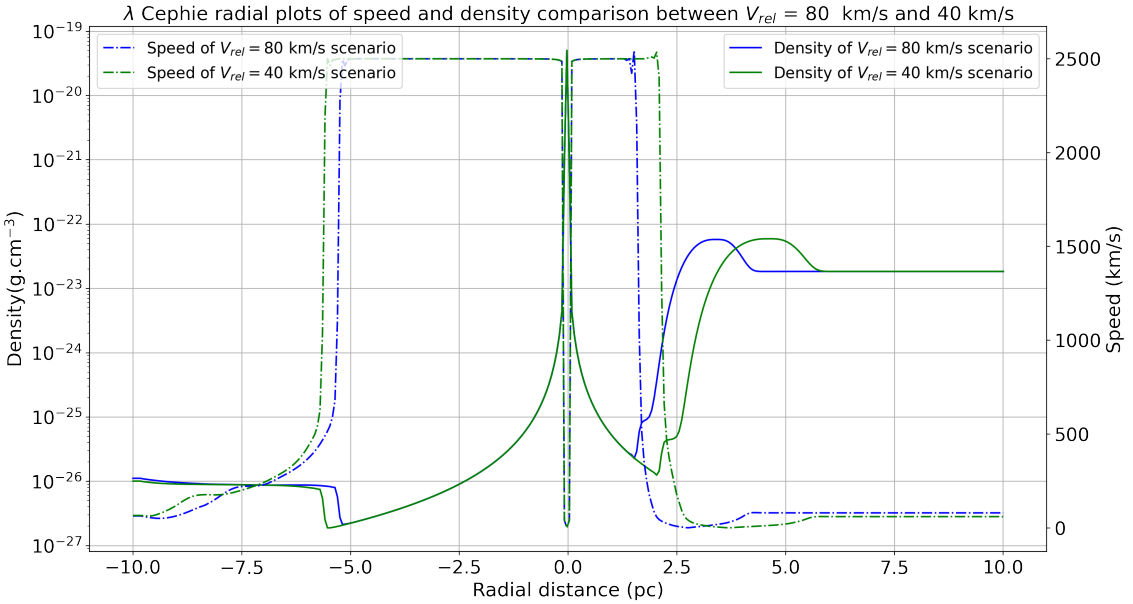

Figure 5.6: *Density and outflow comparison between V_{rel} = 80 km/s and V_{rel} = 40 km/s. These figures are taken from Figures 5.5(a) and 5.5(b).*

the model for the ISM magnetic strength due to the increased computed ISM magnetic field strength. The ISM pressure pushes the ram pressure inward, creating a smaller asymmetrical astrosphere. The inner astrosphere is, therefore, compressed in one hemisphere compared to the other. The orientation and strength of the ISM magnetic field is therefore important parameter in the study of the astrosphere as shown here.

Figure 5.8 shows the density as a contour plot for the computed ISM magnetic field strength scenario of 10^{-7} G. The effects of a high ISM magnetic field strength on the density distribution are defined when compared to Figure 5.5(a). It creates an asymmetrical astrosphere as the total ISM pressure increases with an increase in the ISM magnetic field. The ISM pressure pushes the ram pressure inwards, thus dominating the ram pressure in this area. Note that this effect is similar to that discussed by Opher et al. (2006) for the heliosphere.

5.8 Summary and Conclusions

This chapter presents the astrosphere λ Cephei, as discussed by Scherer et al. (2016b). Observations, as shown by Baalmann et al. (2020), are shown in Figure 5.1. These images showed the southeastern location of the astropause and bow shock. However, the inner astrospheric structure remains invisible due to low density, as

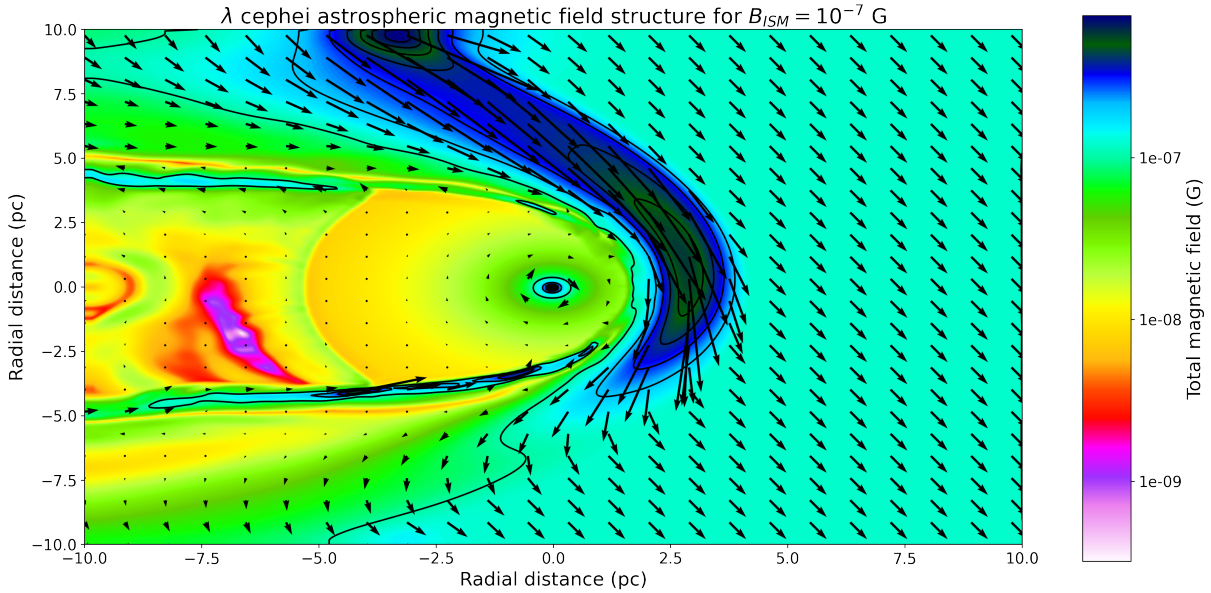

(a) Contour plot in the azimuthal plane showing magnetic field strength for $B_{ISM} = 10^{-7}$ G.

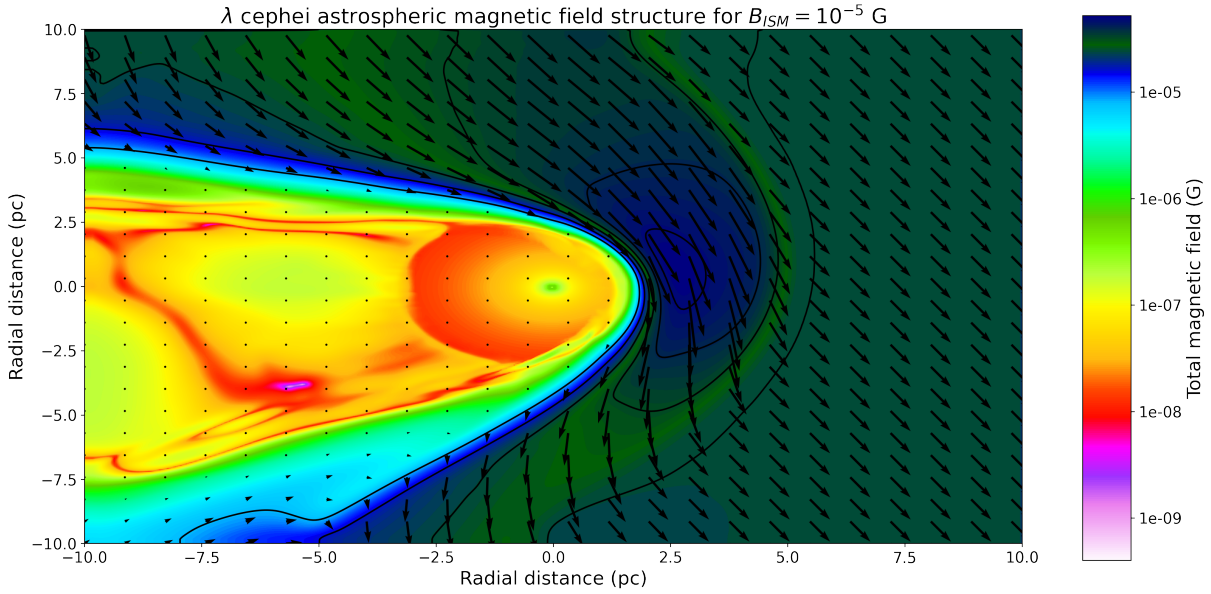

(b) Contour plot in the azimuthal plane showing magnetic field strength for $B_{ISM} = 10^{-5}$ G.

Figure 5.7: *Computed λ Cephei astrospheric magnetic field and ISM magnetic field are shown in the azimuthal plane as contour plots.*

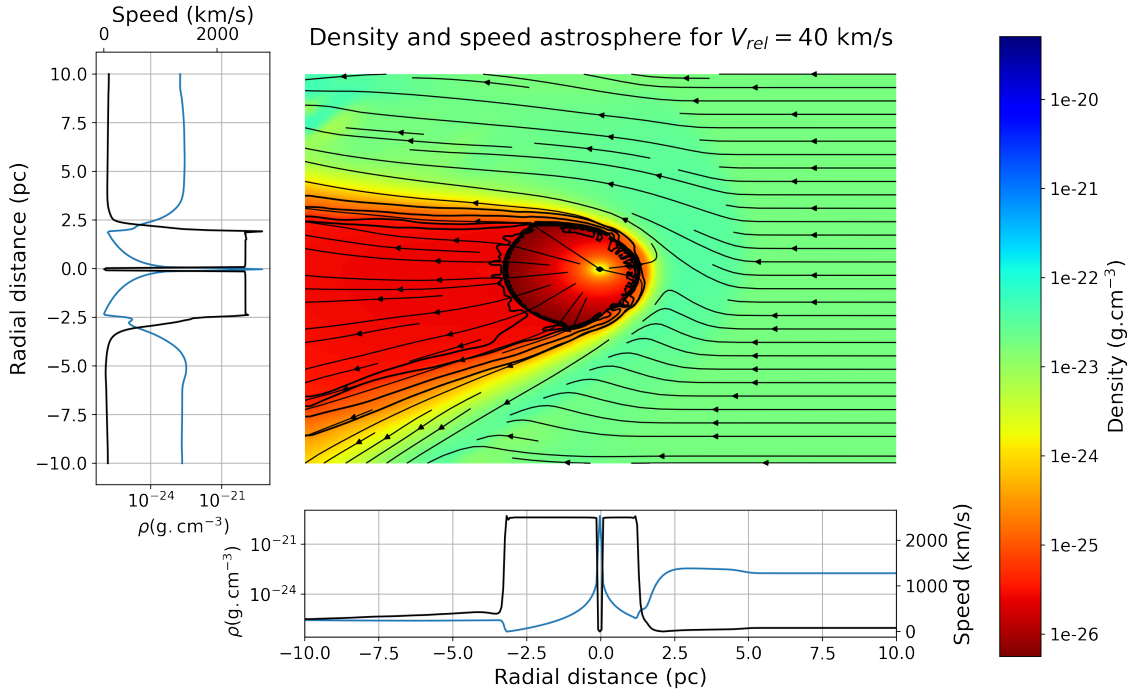

Figure 5.8: *Computed density and outflow speed in the azimuthal plane using the Pen et al. (2003) model. In this scenario* $B_{ISM} = 10^{-5}$ *G.*

discussed by Scherer et al. (2020). The simulation of the λ Cephei's astrosphere was presented using the Cronos model, see Scherer et al. (2016b, 2020) and Baalmann et al. (2021). A comparison between the Cronos model and results from the Pen et al. (2003) model for λ Cephei was shown in Figure 5.4. The Pen et al. (2003) model showed a much smoother transition from supersonic to subsonic. Also, the absence of radiative cooling in the Pen et al. (2003) model resulted in a thicker outer shell. However, the smoother profile was mainly due to the coarse grid assumed in the model.

The effect of decreasing the star's relative velocity was shown in Figure 5.5, using the Pen et al. (2003) model. This figure shows that reducing the velocity results in the expansion of the astrosphere, with the most significant difference observed at the bow shock. Additionally, the effect of the ISM magnetic field strength and orientation is indicated in Figure 5.7. For a high computed ISM magnetic field strength, asymmetry in the computed astrosphere is evident, as shown in Figure 5.8, concluding that the field strength and orientation are important parameters to consider.

Chapter 6

Summary and Conclusion

This study simulated an astrospheric structure to demonstrate how different parameters affect the evolution of the astrosphere and to calculate the astrospheric structure of λ Cephei and compare it to another calculation. The 2D MHD model of Fahr and Kausch (2000), Scherer and Ferreira (2005) and Ferreira and de Jager (2008) were used in Chapter 4, with the same results as the three-dimensional magnetohydrodynamic models of Pen et al. (2003) and Kissmann et al. (2018) shown in Chapter 5.

In this dissertation the Chapters are divided as follows:

In Chapter 4, the 2D MHD was used to investigate the parameters that affect the evolution of the astrosphere; these included the simulation time, mass loss rate, stellar wind outflow speed, ISM density, ISM magnetic field, and ISM temperature.

The computed radial profile at four different simulation times showed how the astrosphere developed with simulation times showing a more developed, astrospheric structure. Simulations corresponding to four different mass loss rates showed that the mass loss rate affected the evolution of the astrosphere by either increasing or decreasing its size. As the mass loss rate increased, the density at the inner boundary also increased; therefore, the ram pressure also increased, thus increasing the size of the astrosphere.

The stellar wind outflow speed of three different outflow speeds showed how this parameter affected the evolution of the astrosphere. For slower outflow speeds, the astrosphere size decreased; hence, the position of the termination shock, the astropause and the bow shock is close to the inner boundary. The stellar wind travels

further at the highest outflow speed scenario, leading to a larger astrosphere. Cooling also occurred late for the high outflow speed scenario. The previous scenario, a thin, high-dense area is visible near the astropause, and for the other scenarios, cooling had already taken place, and the thin shell is now relaxed at the specified simulation time shown. Furthermore, the temperature decreased for all outflow speed scenarios until termination shock. After the termination shock, the temperature increased with the lower SW outflow speed having the lowest temperatures compared to the high-speed scenarios, due to the kinetic energy, which converted to thermal energy. A cool astrosheath was visible close to the bow shock for the high outflow speed scenario.

The simulation of three different ISM densities showed that this parameter decreased the size of the astrosphere as it evolved. In the case of a larger ISM density scenario, the astrosphere size was smaller, with the IAS region shrinking. The compression ratio as a function of the simulation time shows that the higher the ISM density, the lower the compression ratio in the first 50000 years due to cooling.

The effect of three different ISM magnetic field strength scenarios showed that this parameter also affects the outer structure of the astrosphere. A high ISM magnetic field strength contributes to the total ISM pressure, leading to a smaller astrosphere.

Simulations of three different ISM temperatures showed that the parameter affects the position and compression of the BS.

Chapter 5 showed images of λ Cephei reproduced by Baalmann et al. (2020). These images of this particular star showed astropause and a bow shock. However, because the low density and thermal temperature in IAS were not within the range of the instruments, the inner astrospheric structure was not visible. However, the simulations performed by Scherer et al. (2016b, 2020) and Baalmann et al. (2021) calculated the astrospheric structure using limited observations. A comparison was made between the simulation of Scherer et al. (2016b, 2020), Baalmann et al. (2021) and the results of the Pen et al. (2003) model.These are in good agreement apart from the bow shock width being different. The previously mentioned could be caused by radiative cooling, as the Pen et al. (2003) model does not include this effect, or it is more likely because of the Cartesian grid assumed in the Pen et al. (2003) model. Note that the simulation results from Scherer et al. (2016b, 2020), Baalmann et al. (2021) are the most precise.

The effect of the relative velocity and ISM magnetic field on the structure of λ Cephei was calculated using the Pen et al. (2003) model. When the relative velocity

decreased from 80 km/s to 40 km/s, the size of the astrosphere increased. Additionally, in the case of a low ISM magnetic field strength, the orientation of the ISM magnetic field does not affect the simulations. When the ISM magnetic increases notably, however, the orientation becomes important.

Bibliography

Aschwanden, M. (2006). *Physics of the solar corona: an introduction with problems and solutions.* Springer Praxis Books. Springer Berlin Heidelberg.

Baalmann, L. R., Scherer, K., Fichtner, H., Kleimann, J., Bomans, D. J., and Weis, K. (2020). Skymaps of observables of three-dimensional magnetohydrodynamic astrosphere models. *Astronomy and Astrophysics*, 634:A67.

Baalmann, L. R., Scherer, K., Kleimann, J., Fichtner, H., Bomans, D. J., and Weis, K. (2021). Simulating observable structures due to a perturbed interstellar medium in front of astrospheric bow shocks in 3d mhd. *Astronomy and Astrophysics*, 650:A36.

Babcock, H. W. (1961). The topology of the Sun's magnetic field and the 22-year cycle. *Astrophysical Journal*, 133:572.

Balbus, S. A. and Latter, H. N. (2010). The tachocline and differential rotation in the sun. *Monthly Notices of the Royal Astronomical Society*, 407(4):2565–2574.

Baranov, V. B. and Zaitsev, N. A. (1995). On the problem of the solar wind interaction with magnetized interstellar plasma. *Astronomy and Astrophysics*, 304:631.

Barentsen, G., Farnhill, H. J., Drew, J. E., González-Solares, E. A., Greimel, R., Irwin, M. J., Miszalski, B., Ruhland, C., Groot, P., Mampaso, A., Sale, S. E., Henden, A. A., Aungwerojwit, A., Barlow, M. J., Carter, P. J., Corradi, R. L. M., Drake, J. J., Eislöffel, J., Fabregat, J., Gänsicke, B. T., Gentile Fusillo, N. P., Greiss, S., Hales, A. S., Hodgkin, S., Huckvale, L., Irwin, J., King, R., Knigge, C., Kupfer, T., Lagadec, E., Lennon, D. J., Lewis, J. R., Mohr-Smith, M., Morris, R. A. H., Naylor, T., Parker, Q. A., Phillipps, S., Pyrzas, S., Raddi, R., Roelofs, G. H. A., Rodríguez-Gil, P., Sabin, L., Scaringi, S., Steeghs, D., Suso, J., Tata, R., Unruh, Y. C., van Roestel, J., Viironen, K., Vink, J. S., Walton, N. A., Wright, N. J., and Zijlstra, A. A. (2014). The second data release of the INT Photometric Hα Survey of the Northern Galactic Plane (IPHAS DR2). *Monthly Notices of the Royal Astronomical Society*, 444(4):3230–3257.

Beck, J. G. (2000). A comparison of differential rotation measurements–(invited review). *Solar physics*, 191(1):47–70.

Beck, R. (2009). Galactic and extragalactic magnetic fields - a concise review. *Astrophysics and Space Sciences Transactions*, 5(1):43–47.

Biermann, L. (1957). Solar corpuscular radiation and the interplanetary gas. *The Observatory*, 77:109–110.

Blaauw, A. (1961). On the origin of the O- and B-type stars with high velocities (the "run-away" stars), and some related problems. *Bulletin of the Astronomical Institutes of the Netherlands*, 15:265.

Bouret, J. C., Hillier, D. J., Lanz, T., and Fullerton, A. W. (2012). Properties of galactic early-type o-supergiants-a combined fuv-uv and optical analysis. *Astronomy and Astrophysics*, 544:A67.

Bromley, B. C., Kenyon, S. J., Brown, W. R., and Geller, M. J. (2009). Runaway stars, hypervelocity stars, and radial velocity Surveys. *The Astrophysical Journal*, 706(2):925–940.

Burger, R. A. (2005). Cosmic-ray modulation and the heliospheric magnetic field. *Advances in Space Research*, 35(4):636–642.

Burlaga, L. F., Ness, N., Acuña, M., Lepping, R. P., Connerney, J. E. P., and Richardson, J. D. (2008). Magnetic fields at the solar wind termination shock. *Nature*, 454:75–7.

Burlaga, L. F. and Ness, N. F. (1993). Large-scale distant heliospheric magnetic field: Voyager 1 and 2 observations from 1986 through 1989. *Journal of Geophysical Research*, 98(A10):17451–17460.

Cassinelli, J. P. and Lamers, H. J. G. L. M. (1987). Winds from hot young stars. In Kondo, Y. and Wamsteker, W., editors, *Exploring the Universe with the IUE Satellite*, volume 129 of *Astrophysics and Space Science Library*, page 139.

Chaisson, E., McMillan, S., and Rice, E. (2005). *Astronomy today.* Pearson/Prentice Hall Upper Saddle River, NJ.

Choudhuri, A. R. (1998). *The physics of fluids and plasmas : An introduction for astrophysicists.*

Chu, F., Langendorf, S. J., Olson, J., Byvank, T., Endrizzi, D. A., LaJoie, A. L., McCollam, K. J., and Forest, C. B. (2023). Characterization of fast magnetosonic waves driven by compact toroid plasma injection along a magnetic field. *Physics of Plasmas*, 30(12).

Corti, G., Poletto, G., Romoli, M., Michels, J., Kohl, J., and Noci, G. (1997). Physical parameters in plume and interplume regions from UVCS observations. In Wilson, A., editor, *Fifth SOHO Workshop: The Corona and Solar Wind Near Minimum Activity.*, volume 404 of *ESA Special Publication*, page 289.

Cowie, L. L., McKee, C. F., and Ostriker, J. P. (1981). Supernova remnant revolution in an inhomogeneous medium. I - Numerical models. *Astrophysical Journal*, 247:908–924.

Cranmer, S. R. (2002). Coronal holes and the high-speed solar wind. *Space science reviews*, 101:229–294.

Cranmer, S. R. and Winebarger, A. R. (2019). The properties of the solar corona and its connection to the solar wind. *Annual Review of Astronomy and Astrophysics*, 57:157–187.

Crowther, P. A. (2007). Physical properties of Wolf-Rayet stars. *Annual Review of Astronomy and Astrophysics*, 45(1):177–219.

Dalgarno, A. and McCray, R. A. (1972). Heating and ionization of hi regions. *Annual Review of Astronomy and Astrophysics*, 10(1):375–426.

Decker, R., Krimigis, S. M., Roelof, E. C., Hill, M. E., Armstrong, T., Gloeckler, G., Hamilton, D., and Lanzerotti, L. (2005). Voyager 1 in the foreshock, termination shock, and heliosheath. *Science (New York, N.Y.)*, 309:2020–4.

Drew, J. E., Greimel, R., Irwin, M. J., Aungwerojwit, A., Barlow, M. J., Corradi, R. L. M., Drake, J. J., Gänsicke, B. T., Groot, P., Hales, A., Hopewell, E. C., Irwin, J., Knigge, C., Leisy, P., Lennon, D. J., Mampaso, A., Masheder, M. R. W., Matsuura, M., Morales-Rueda, L., Morris, R. A. H., Parker, Q. A., Phillipps, S., Rodriguez-Gil, P., Roelofs, G., Skillen, I., Sokoloski, J. L., Steeghs, D., Unruh, Y. C., Viironen, K., Vink, J. S., Walton, N. A., Witham, A., Wright, N., Zijlstra, A. A., and Zurita, A. (2005). The INT Photometric Hα Survey of the Northern Galactic Plane (IPHAS). *Monthly Notices of the Royal Astronomical Society*, 362(3):753–776.

Dupree, A. K. and Reimers, D. (1987). Mass loss from cool stars. In Kondo, Y. and Wamsteker, W., editors, *Exploring the Universe with the IUE Satellite*, volume 129 of *Astrophysics and Space Science Library*, page 321.

Dyson, J. E. and Williams, D. A. (1997). *The physics of the interstellar medium.*

Esser, R., Habbal, S. R., Coles, W. A., and Hollweg, J. V. (1997). Hot protons in the inner corona and their effect on the flow properties of the solar wind. *Journal of Geophysical Research*, 102(A4):7063–7074.

Evans, C. R. and Hawley, J. F. (1988). Simulation of magnetohydrodynamic flows-a constrained transport method. *Astrophysical Journal*, 332:659–677.

Fahr, H. J. and Kausch, T.and Scherer, H. (2000). A 5-fluid hydrodynamic approach to model the solar system-interstellar medium interaction. *Astronomy and Astrophysics*, 357:268–282.

Fahr, H. J. and Neutsch, W. (1983). Stationary plasma-field equilibrium states in astropause boundary layers. I - general theory. *Monthly Notices of the Royal Astronomical Society*, 205:839–857.

Fahr, H. J., Neutsch, W., Grzedzielski, S., Macek, W., and Ratkiewicz-Landowska, R. (1986). Plasma transport across the heliopause. *Space Science Reviews*, 43(3-4):329–381.

Fahr, H. J. and Scherer, K. (1995). On the motion of wind-driving stars relative to the ambient interstellar medium. *Astrophysics and Space Science*, 225(1):21–45.

Ferreira, S. E. S. and de Jager, O. C. (2008). Supernova remnant evolution in non-uniform media. In *International Cosmic Ray Conference*, volume 2 of *International Cosmic Ray Conference*, pages 593–596.

Ferreras, I. (2019). *Fundamentals of galaxy dynamics, formation and discovery.* University College London Press.

Finlay, C. (2007). *Alfvén Waves*, pages 3–6. Springer Netherlands, Dordrecht.

Frisch, P. C. (1993). G-Star astropauses: a test for interstellar pressure. *Astrophysical Journal*, 407:198.

Gaia Collaboration (2018). VizieR Online Data Catalog: Gaia DR2 (Gaia Collaboration, 2018). *VizieR Online Data Catalog*, page I/345.

Giacalone, J. (1999). Particle transport and acceleration at corotating interaction regions. *Advances in Space Research*, 23(3):581–590.

Gies, D. R. (1987). The kinematical and binary properties of association and field O stars. *Astrophysical Journal*, 64:545.

Gnat, O. and Ferland, G. J. (2012). Ion-by-ion cooling efficiencies. *Astrophysical Journal*, 199(1):20.

Hale, G. E. (1908). On the probable existence of a magnetic field in sun-spots. *Astrophysical Journal*, 28:315.

Hartmann, L. (2009). *Accretion processes in star formation: Second edition.* Cambridge University Press.

Hattingh, M. (1998). *The modulation of galactic cosmic rays in a three-dimensional heliosphere.* PhD thesis, North West University.

Heerikhuisen, J. and Pogorelov, N. V. (2011). The influence of the interstellar magnetic field on the IBEX ribbon. In *AGU Fall Meeting Abstracts*, volume 2011, pages SH14A–06.

Herbst, K., Baalmann, L. R., Bykov, A., Engelbrecht, N. E., Ferreira, S. E. S., Izmodenov, V. V., Korolkov, S. D., Levenfish, K. P., Linsky, J. L., Meyer, D. M., et al. (2022). Astrospheres of planet-hosting cool stars and beyond · when modeling meets observations. *Space Science Reviews*, 218(4):29.

Herbst, K., Scherer, K., Ferreira, S. E. S., Baalmann, L. R., Engelbrecht, N. E., Fichtner, H., Kleimann, J., Strauss, R. D. T., Moeketsi, D. M., and Mohamed, S. (2020). On the diversity of m-star astrospheres and the role of galactic cosmic rays within. *The Astrophysical Journal Letters*, 897(2):L27.

Hoeksema, J. T., Wilcox, J. M., and Scherrer, P. H. (1983). The structure of the heliospheric current sheet: 1978-1982. *Journal of Geophysical Research: Space Physics*, 88(A12):9910–9918.

Holzer, T. E. (1989). Interaction between the solar wind and the interstellar medium. *Annual Review of Astronomy and Astrophysics*, 27:199–234.

Hoogerwerf, R., de Bruijne, J. H. J., and de Zeeuw, P. T. (2001). On the origin of the O and B-type stars with high velocities. II. Runaway stars and pulsars ejected from the nearby young stellar groups. *Astronomy and Astrophysics*, 365:49–77.

Huang, G. H., Lin, C. H., and Lee, L. C. (2017). Solar open flux migration from pole to pole: Magnetic field reversal. *Scientific reports*, 7(1):9488.

Hundhausen, A. J. (1972). Interplanetary shock waves and the structure of solar wind disturbances. In Sonett, C. P., Coleman, P. J., and Wilcox, J. M., editors, *NASA Special Publication*, volume 308, page 393.

Izmodenov, V.and Gangopadhyay, P., Gruntman, M., and Judge, D. (2003). Interstellar pioneer 10 euv data: Possible constraints on the local interstellar parameters. In *AIP Conference Proceedings*, volume 679. American Institute of Physics.

Jin, S. and Xin, Z. (1995). The relaxation schemes for systems of conservation laws in arbitrary space dimensions. *Communications on Pure and Applied Mathematics*, 48(3):235–276.

Jokipii, J. R. and Kota, J. (1989). The polar heliospheric magnetic field. *Geophysical research letters*, 16(1):1–4.

Kissmann, R., Kleimann, J., Krebl, B., and Wiengarten, T. (2018). The CRONOS Code for astrophysical magnetohydrodynamics. *Astrophysical Journal*, 236(2):53.

Kivelson, M. G., Russell, C. T., and Cowley, S. W. H. (1995). Introduction to space physics. *The Observatory*, 115:353.

Krieger, A. S., Timothy, A. F., and Roelof, E. C. (1973). A coronal hole and its identification as the source of a high velocity solar wind stream. *Solar Physics*, 29(2):505–525.

Langner, U. and Potgieter, M. (2004). Effects of the solar wind termination shock and heliosheath on the heliospheric modulation of galactic and anomalous helium. *Annales Geophysicae*, 22(8):3063–3072.

Langner, U., Potgieter, M., Fichtner, H., and Borrmann, T. (2006). Modulation of anomalous protons: effects of different solar wind speed profiles in the heliosheath. *Journal of Geophysical Research*, 111.

Light, J. (2020). *Numerical modelling of astrospheres.* Dissertation, North West University.

Light, J., Ferreira, S. E. S., Engelbrecht, N. E., Scherer, K., and Herbst, K. (2022). On the numerical modelling of astrospheres, including those of luminous blue variable stars, and the modulation of cosmic rays within. *Monthly Notices of the Royal Astronomical Society*, 516(3):3284–3296.

Lykins, M. L., Ferland, G. J., Porter, R. L., van Hoof, P. A. M., Williams, R. J. R., and Gnat, O. (2013). Radiative cooling in collisionally ionized and photoionized plasmas. *Monthly Notices of the Royal Astronomical Society*, 429(4):3133–3143.

Marais, A. (2023). *The numerical simulation of astrospheric evolution in different interstellar environments.* Dissertation, North West University.

McClintock, B. H., Norton, A. A., and Li, J. (2014). Re-examining sunspot tilt angle to include anti-Hale statistics. *Astrophysical Journal*, 797(2):130.

McComas, D. J., Alexashov, D., Bzowski, M., Fahr, H., Heerikhuisen, J., Izmodenov, V., Lee, M. A., Möbius, E., Pogorelov, N., Schwadron, N. A., et al. (2012a). The heliosphere's interstellar interaction: No bow shock. *Science*, 336(6086):1291–1293.

McComas, D. J., Alexashov, D., Bzowski, M., Fahr, H., Heerikhuisen, J., Izmodenov, V., Lee, M. A., Möbius, E., Pogorelov, N., Schwadron, N. A., and Zank, G. P. (2012b). The heliosphere's interstellar interaction: No bow shock. *Science*, 336(6086):1291.

McComas, D. J., Allegrini, F., Bochsler, P., Bzowski, M., Christian, E. R., Crew, G. B., DeMajistre, R., Fahr, H., Fichtner, H., Frisch, P. C., Funsten, H. O., Fuselier, S. A., Gloeckler, G., Gruntman, M., Heerikhuisen, J., Izmodenov, V., Janzen, P., Knappenberger, P., Krimigis, S., Kucharek, H., Lee, M., Livadiotis, G., Livi, S., MacDowall, R. J., Mitchell, D., Möbius, E., Moore, T., Pogorelov, N. V., Reisenfeld, D., Roelof, E., Saul, L., Schwadron, N. A., Valek, P. W., Vanderspek, R., Wurz, P., and Zank, G. P. (2009). Global observations of the interstellar interaction from the interstellar boundary explorer (IBEX). *Science*, 326(5955):959.

Mellema, G. and Lundqvist, P. (2002). Stellar wind bubbles around WR and [WR] stars. *Astronomy and Astrophysics*, 394:901–909.

Miesch, M. S., Brun, A. S., and Toomre, J. (2006). Solar differential rotation influenced by latitudinal entropy variations in the tachocline. *The Astrophysical Journal*, 641(1):618.

Moore, R. and Rabin, D. (1985). Sunspots. *Annual Review of Astronomy and Astrophysics*, 23:239–266.

Moraal, H. (1990). Proton modulation near solar minimum periods in consecutive solar cycles. In *21st International Cosmic Ray Conference (ICRC21)*, volume 6 of *International Cosmic Ray Conference*, page 140.

Morgan, W. W. and Keenan, P. C. (1973). Spectral classification. *Annual Review of Astronomy and Astrophysics*, 11:29.

Moss, D. (1992). Magnetic fields and differential rotation in stars. *Monthly Notices of the Royal Astronomical Society*, 257(4):593–601.

Muñoz-Jaramillo, A., Navarrete, B., and Campusano, L. E. (2021). Solar anti-Hale bipolar magnetic regions: a distinct population with systematic properties. *Astrophysical Journal*, 920(1):31.

Neupert, W. M. and Pizzo, V. (1974). Solar coronal holes as sources of recurrent geomagnetic disturbances. In *Bulletin of the American Astronomical Society*, volume 6, page 292.

Norton, A., Howe, R., Upton, L., and Usoskin, I. (2023). Solar cycle observations. *Space Science Reviews*, page arXiv:2305.19803.

Ofman, L. (2004). The origin of the slow solar wind in coronal streamers. *Advances in Space Research*, 33:681–688.

Opher, M., Stone, E. C., and Liewer, P. C. (2006). The effects of a local interstellar magnetic field on Voyager 1 and 2 observations. *Astrophysical Journall*, 640(1):L71–L74.

Owens, M. and Forsyth, R. (2013). The heliospheric magnetic field. *Living Reviews in Solar Physics*, 10(1):5.

Parker, E. N. (1958). Dynamics of the interplanetary gas and magnetic fields. *Astrophysical Journal*, 128:664.

Parker, E. N. (1963). *Interplanetary dynamical processes.*

Pen, U., Arras, P., and Wong, S. (2003). A free, fast, simple, and efficient total variation diminishing magnetohydrodynamic code. *Astrophysical Journal*, 149(2):447–455.

Perets, H. B. and Šubr, L. (2012). The properties of dynamically ejected runaway and hyper-runaway stars. *Astrophysical Journal*, 751(2):133.

Phillips, J. L., Bame, S. J., Barnes, A., Barraclough, B. L., Feldman, W. C., Goldstein, B. E., Gosling, J. T., Hoogeveen, G. W., McComas, D. J., Neugebauer, M., and Suess, S. T. (1995). Ulysses solar wind plasma observations from pole to pole. *Geophysical research letters*, 22(23):3301–3304.

Pogorelov, N. V., Heerikhuisen, J., Zank, G. P., and Borovikov, S. N. (2009). Influence of the interstellar magnetic field and neutrals on the shape of the outer heliosphere. *Space Science Reviews*, 143(1-4):31–42.

Pogorelov, N. V., Heerikhuisen, J., Zank, G. P., Borovikov, S. N., Frisch, P. C., and McComas, D. J. (2011). Interstellar boundary explorer measurements and magnetic field in the vicinity of the heliopause. *Astrophysical Journal*, 742(2):104.

Pogorelov, N. V., Stone, E. C., Florinski, V., and Zank, G. P. (2007). Termination shock asymmetries as seen by the Voyager spacecraft: The role of the interstellar magnetic field and neutral hydrogen. *Astrophysical Journal*, 668(1):611–624.

Richardson, A. S. (2019). *2019 NRL plasma formulary*. Naval Research Laboratory Washington.

Richardson, J., Kasper, J., Li, W., Belcher, J., and Lazarus, A. (2008). Cool heliosheath plasma and deceleration of the upstream solar wind at the termination shock. *Nature*, 454:63–6.

Richardson, J. D., Burlaga, L. F., Elliott, H., Kurth, W. S., Liu, Y. D., and von Steiger, R. (2022). Observations of the outer heliosphere, heliosheath, and interstellar medium. *Space Science Reviews*, 218(4):35.

Rieke, G. H., Young, E. T., Engelbracht, C. W., Kelly, D. M., Low, F. J., Haller, E. E., Beeman, J. W., Gordon, K. D., Stansberry, J. A., Misselt, K. A., Cadien, J., Morrison, J. E., Rivlis, G., Latter, W. B., Noriega-Crespo, A., Padgett, D. L., Stapelfeldt, K. R., Hines, D. C., Egami, E., Muzerolle, J., Alonso-Herrero, A., Blaylock, M., Dole, H., Hinz, J. L., Le Floc'h, E., Papovich, C., Pérez-González, P. G., Smith, P. S., Su, K. Y. L., Bennett, L., Frayer, D. T., Henderson, D., Lu, N., Masci, F., Pesenson, M., Rebull, L., Rho, J., Keene, J., Stolovy, S., Wachter, S., Wheaton, W., Werner, M. W., and Richards, P. L. (2004). The Multiband Imaging Photometer for Spitzer (MIPS). *The Astrophysical Journal Supplement Series*, 154(1):25–29.

Russell, H. N. (1914). Relations between the spectra and other characteristics of the stars. *Popular Astronomy*, 22:275–294.

Scherer, K., Baalmann, L. R., Fichtner, H., Kleimann, J., Bomans, D. J., Weis, K., Ferreira, S. E. S., and Herbst, K. (2020). Mhd-shock structures of astrospheres: λ cephei-like astrospheres. *Monthly Notices of the Royal Astronomical Society*, 493(3):4172–4185.

Scherer, K., Bomans, D. J., Ferreira, S. E. S., Fichtner, H., Kleimann, J., Strauss, R. D., and Weis, K. (2016a). Comparison of astrospheres around cool and hot stars. In *Journal of Physics Conference Series*, volume 767 of *Journal of Physics Conference Series*, page 012024.

Scherer, K. and Ferreira, S. E. S. (2005). A heliospheric hybrid model: Hydrodynamic plasma flow and kinetic cosmic ray transport. *Astrophysics and Space Sciences Transactions*, 1:17–27.

Scherer, K. and Fichtner, H. (2014). The return of the bow shock. *Astrophysical Journal*, 782(1):25.

Scherer, K., Fichtner, H., Kleimann, J., Wiengarten, T., Bomans, D. J., and Weis, K. (2016b). Shock structures of astrospheres. *Astronomy and Astrophysics*, 586:A111.

Scherer, K., Fichtner, H., and Marsch, E. (2000). Preface (the outer heliosphere: beyond the planets.). In Scherer, K., Fichtner, H., and Marsch, E., editors, *The Outer Heliosphere: Beyond the Planets*, page 5.

Scherer, K., Fichtner, H., Strauss, R. D., Ferreira, S. E. S., Potgieter, M. S., and Fahr, H.-J. (2011). On cosmic ray modulation beyond the heliopause: where is the modulation boundary. *The Astrophysical Journal*, 735(2):128.

Scherer, K., van der Schyff, A., Bomans, D. J., Ferreira, S. E. S., Fichtner, H., Kleimann, J., Strauss, R. D., Weis, K., Wiengarten, T., and Wodzinski, T. (2015a). Cosmic rays in astrospheres. *Astronomy and Astrophysics*, 576:A97.

Scherer, K., van der Schyff, A., Bomans, D. J., Ferreira, S. E. S., Fichtner, H., Kleimann, J., Strauss, R. D., Weis, K., Wiengarten, T., and Wodzinski, T. (2015b). Cosmic rays in astrospheres. *Astronomy and Astrophysics*, 576:A97.

Schure, K. M., Kosenko, D., Kaastra, J. S., Keppens, R., and Vink, J. (2009). A new radiative cooling curve based on an up-to-date plasma emission code. *Astronomy and Astrophysics*, 508(2):751–757.

Schwenn, R. (1983). The "average" solar wind in the inner heliosphere: structures and slow variations. In *NASA Conference Publication*, volume 228 of *NASA Conference Publication*, page 0.489.

Schwenn, R. (1986). Relationship of coronal transients to interplanetary shocks - 3d aspects. *Space Science Reviews*, 44(1-2):139–168.

Schwenn, R. (2006). Solar wind sources and their variations over the solar cycle. *Space science reviews*, 124:51–76.

Sheeley, N. R., Wang, Y. M., Hawley, S. H., Brueckner, G. E., Dere, K. P., Howard, R. A., Koomen, M. J., Korendyke, C. M., Michels, D. J., Paswaters, S. E., Socker, D. G., St. Cyr, O. C., Wang, D., Lamy, P. L., Llebaria, A., Schwenn, R., Simnett,

G. M., Plunkett, S., and Biesecker, D. A. (1997). Measurements of flow speeds in the corona between 2 and 30 $R_{\odot}$. *Astrophysical Journal*, 484(1):472–478.

Smith, C. W. and Bieber, J. W. (1991). Solar Cycle Variation of the Interplanetary Magnetic Field Spiral. *Astrophysical Journal*, 370:435.

Smith, E. J. (1989). Interplanetary magnetic field over two solar cycles and out to 20 au. *Advances in Space Research*, 9(4):159–169.

Smith, E. J. (1990). Magnetic fields in the heliosphere: Pioneer observations. In Grzedzielski, S. and Page, D. E., editors, *Physics of the Outer Heliosphere.*, pages 253–265.

Smith, E. J. (2001). The heliospheric current sheet. *Journal of Geophysical Research*, 106(A8):15819–15832.

Smith, E. J. and Marsden, R. G. (1995). Ulysses observations from pole-to-pole: An introduction. *Geophysical research letters*, 22(23):3297–3300.

Solanki, S. K. (2003). Sunspots: an overview. *Astronomy and Astrophysics*, 11(2-3):153–286.

Solanki, S. K. (2007). Solar magnetic fields: an introduction. In *Space Solar Physics: Theoretical and observational issues in the context of the SOHO mission proceedings of a summer school held in orsay.*, pages 41–75. Springer.

Stone, E. C., Cummings, A. C., Mcdonald, F. B., Heikkila, B. C., Lal, N. K., and Webber, W. R. (2005). Voyager 1 explores the termination shock region and the heliosheath beyond. *Science*, 309:2017 – 2020.

Stone, E. C., Cummings, A. C., Mcdonald, F. B., Heikkila, B. C., Lal, N. K., and Webber, W. R. (2008). An asymmetric solar wind termination shock. *Nature*, 454:71–74.

Strauss, R. D. and Potgieter, M. S. (2010). Modeling anomalous cosmic ray oxygen gradients over successive solar cycles. *Journal of Geophysical Research (Space Physics)*, 115(A12):A12111.

Strauss, R. D. T. (2013). *Modelling of cosmic ray modulation in the heliosphere by stochastic processes.* PhD thesis, North West University(Potchefstroom campus).

Sutherland, R. S. and Dopita, M. A. (1993). Cooling functions for low-density astrophysical plasmas. *Astrophysical Journal*, 88:253.

Sébastien, G. (2016). *Introduction to modern magnetohydrodynamics.* Cambridge University Press.

Temmer, M., Rybák, J., Bendík, P., Veronig, A., Vogler, F., Otruba, W., Pötzi, W., and Hanslmeier, A. (2006). Hemispheric sunspot numbers $\{R_n\}$ and $\{R_s\}$ from 1945-2004: catalogue and N-S asymmetry analysis for solar cycles 18-23. *Astronomy and Astrophysics*, 447(2):735–743.

Usoskin, I. G. (2008). A history of solar activity over millennia. *Living Reviews in Solar Physics*, 5.

van Marle, A. J. and Keppens, R. (2011). Radiative cooling in numerical astrophysics: The need for adaptive mesh refinement. *Computers and Fluids*, 42(1):44–53.

van Marle, A. J., Meliani, Z., and Marcowith, A. (2015). Shape and evolution of wind-blown bubbles of massive stars: On the effect of the interstellar magnetic field. *Astronomy and Astrophysics*, 584:A49.

Wang, Y. M. (2012). Semi empirical models of the slow and fast solar wind. *Space science reviews*, 172:123–143.

Weaver, R., McCray, R., Castor, J., Shapiro, P., and Moore, R. (1977). Interstellar bubbles. II. structure and evolution. *Astrophysical Journal*, 218:377–395.

Werner, M. W., Roellig, T. L., Low, F. J., Rieke, G. H., Rieke, M., Hoffmann, W. F., Young, E., Houck, J. R., Brandl, B., Fazio, G. G., Hora, J. L., Gehrz, R. D., Helou, G., Soifer, B. T., Stauffer, J., Keene, J., Eisenhardt, P., Gallagher, D., Gautier, T. N., Irace, W., Lawrence, C. R., Simmons, L., Van Cleve, J. E., Jura, M., Wright, E. L., and Cruikshank, D. P. (2004). The Spitzer Space Telescope Mission. *The Astrophysical Journal Supplement Series*, 154(1):1–9.

Wilcox, J. M. and Ness, N. F. (1965). Quasi-stationary corotating structure in the interplanetary medium. *Journal of Geophysical Research*, 70(23):5793–5805.

Withbroe, G. L., Feldman, W. C., and Ahluwalia, H. S. (1991). The solar wind and its coronal origins. In *Solar Interior and Atmosphere*, pages 1087–1106.

Wright, E. L., Eisenhardt, P. R. M., Mainzer, A. K., Ressler, M. E., Cutri, R. M., Jarrett, T., Kirkpatrick, J. D., Padgett, D., McMillan, R. S., Skrutskie, M., Stanford, S. A., Cohen, M., Walker, R. G., Mather, J. C., Leisawitz, D., Gautier, T. N., I., McLean, I., Benford, D., Lonsdale, C. J., Blain, A., Mendez, B., Irace, W. R., Duval, V., Liu, F., Royer, D., Heinrichsen, I., Howard, J., Shannon, M.,

Kendall, M., Walsh, A. L., Larsen, M., Cardon, J. G., Schick, S., Schwalm, M., Abid, M., Fabinsky, B., Naes, L., and Tsai, C. (2010). The Wide-field Infrared Survey Explorer (WISE): Mission description and initial on-orbit performance. *Astronomical Journal*, 140(6):1868–1881.

Zan, G. P. (1999). Interaction of the solar wind with the local interstellar medium: A theoretical perspective. *Space Science Reviews*, 89(3-4):413–688.

Zank, G. P. (2015). Faltering steps into the galaxy: The boundary regions of the heliosphere. *Annual Review of Astronomy and Astrophysics*, 53:449–500.

Zhou, X., Smith, E. J., Winterhalter, D., McComas, D. J., Skoug, R. M., Goldstein, B. E., and Smith, C. W. (2005). Thickness of heliospheric current and plasma sheets: Dependence on distance. In *AGU Spring Meeting Abstracts.*, volume 2005, pages SH41A–01.

Zieger, B., Opher, M., Schwadron, N. A., McComas, D. J., and Tóth, G. (2013). A slow bow shock ahead of the heliosphere. *Geophysical research letters*, 40(12):2923–2928.